Integrated CMOS Polymerase Chain Reaction Lab-on-chip

Haig Stephen Norian

Submitted in partial fulfillment of the

requirements for the degree

of Doctor of Philosophy

in the Graduate School of Arts and Sciences

COLUMBIA UNIVERSITY

2014

Abstract

Integrated CMOS Polymerase Chain Reaction Lab-on-chip

Haig Stephen Norian

Considerable effort has recently been directed toward the miniaturization of quantitative-polymerase-chain-reaction [QPCR] instrumentation in an effort to reduce both cost and form factor for point-of-care applications. Notable gains have been made in shrinking the required volumes of PCR reagents, but resultant prototypes retain their bench-top form factor either due to heavy heating plates or cumbersome optical sensing instrumentation. In this thesis, we describe the use of complementary-metal-oxide semiconductor (CMOS) integrated circuit (IC) technology to produce a fully integrated qPCR lab-on-chip. Exploiting a 0.35-μm high-voltage CMOS process, the IC contains all of the key components for performing qPCR. Integrated resistive heaters and temperature sensors regulate the surface temperature of the chip to 0.45°C. Electrowetting-on-dielectric microfluidic pixels are actively driven from the chip surface, allowing for droplet generation and transport down to volumes of less than 1.2 nanoliters. Integrated single-photon avalanche diodes [SPAD] are used for fluorescent monitoring of the reaction, allowing for the quantification of target DNA with more than four-orders-of-magnitude of dynamic range with sensitivities down to a single copy per droplet. Using this device, reliable and sensitive real-time proof-of-concept detection of *Staphylococcus aureus* (*S. aureus*) is demonstrated.

Table of Contents

List of Figures

List of Tables:

Acknowledgements

I wish to thank all of those who have provided a guiding hand in the completion of this work. Indeed, they are too many to list, but I'll give it my best shot. First and foremost, I would like to thank my advisor, Professor Kenneth Shepard. Ken's enthusiasm and unbridled energy has provided a shining core both to my graduate years and to the research that I performed. From the first research discussion through the chip tapeout to the final analysis of our collected data, Ken has provided the drive necessary to fully develop the research described in this report.

Special thanks to my co-advisor and thesis sponsor Professor Ioannis John Kymissis, who provided a lab of tools and supplies like none I had seen before. From a thermal evaporator to a 3D printer, the Kymissis Lab had all the research and rapid prototyping tools I could ever wish for. Beyond the exquisite research arsenal, meeting with John helped put my thoughts in order and provide much needed perspective on the project at hand.

Over the course of the last five years, I have benefited immensely from discussions and assistance from all of the members of the Bioelectronic Systems Laboratory as well as the Columbia Lab for Unconventional Electronics, including Ryan Field, Michael Lekas, Noah Sturcken, Hassan Edrees, Eddy Hsu, Vincent Lee, John Sarik, Jacob Rosenstein, Matt Johnston, Nadia Pervez, Steven Warren, Jaebin Choi, Scott Trocchia, Kostas Alexandrou, and Shyuan Yang.

Chapter 1: Introduction

Research into the development of next-generation genetic diagnostic devices for point-of-care use has progressed down two paths.   One type of device seeks to perform the full real-time sequencing of every strand of DNA present within a given biological test sample, such as blood or saliva. The reading of all of the genetic matter in a given sample provides the end-user the ability to generate a complete list of all bacteria or viruses initially present. Although ultimately providing nearly infinite diagnostic information from a single screening, diagnostics based on real-time sequencing technology are still in their infancy. An alternative method of exploiting the vast genetic databases that have been accumulated since the late 1990's is to limit the scope of the sweep.

Instead of determining the full sequences of all of the genetic matter in a test sample, a select, pre-determined set of particular test sequences can be isolated for screening. This method has evolved considerably during the past forty years, from the Southern Blot test developed in by Edwin Southern in 1975 [1], to the Polymerase Chain Reaction (PCR) formulated by Kary Mulls in 1983 [2,3], and more recently to real-time quantitative PCR (QPCR) schemes used in cutting edge devices such the Via7 real-time PCR system [Applied Biosystems, Foster City, CA] [4,5] .

QPCR is a method of selectively amplifying a very specific DNA sequence in a given

test sample using carefully controlled thermal cycling in the presence of a custom cocktail designed for the specific detection of a suspect DNA sequence. Let us consider a DNA sequence that is unique only to the tuberculosis-causing bacterium. If the bacterium of interest is present, so too will its DNA. If the culprit DNA is initially present, the PCR protocol will induce the concentration of the unique-to-tuberculosis segment of DNA to undergo an exponential increase. With the use of fluorescent or chemical tagging, this drastic increase in the concentration of this particular DNA sequence can be monitored in real time and used for diagnostic purposes. If the exponential spike is detected, then a positive diagnosis is registered; otherwise, the test is negative.

PCR instrumentation for such disease diagnosis has proven very successful for the DNA-based detection of specific bacteria, such as Methicillin-resistance Staphylococcus Aureaus (MRSA) and Tuberculosis (TB) [6-9]. Furthermore, over the past two decades, droplet size per PCR reaction has decreased from a milliliter vial down to sub-nanoliter droplets. Despite considerable gains in shrinking the volumes on which each QPCR test is performed, the overall form factor of these devices is still that of a stationary, bench-top device [10-14]. There are several factors that have made the scaling of QPCR instrumentation difficult. First, uniform temperature control has come at the expense of heavy heating blocks. Second, the fluorescent sensing has required bulky and delicate optics to obtain a reliable measurement of the concentration of target DNA. Third, any integrated microfluidics has relied on pneumatic control, regulated by large vacuum pumps. Thus, although very precise readings can be taken, high performance PCR devices sorely lack the point of care form factor.

1.1 Genetic Diagnostics using QPCR

QPCR detection techniques have been used in the diagnosis of methicillin-resistant Staphylococcus species [6,7], tuberculosis [8,9], and Human Immunodeficiency Virus Type 1 [15]. The detection of these bacteria and viruses is a huge step forward for diagnostic technology as the complete detection protocol is performed entirely upon highly specific targets present in volumes that are smaller than a nanoliter.

However, in addition to scaling the volume upon which QPCR is performed, it has become equally important that the rapid-detection QPCR tool itself meet a point of care form factor for increased portability and decreased cost. For instance, studies have shown that patients with STD's are more likely to schedule a voluntary visit for a screening if the results can be directly determined during the visit [16,17]. Fast, low-cost tools capable of high quality genetic based diagnosis in every hospital and clinic would increase a patient's likelihood for more frequent screening. Furthermore, rapid diagnosis in the developing world has demonstrated similar increases in patient compliance [18,19] The faster the tool, the more likely the patient to agree to a screening. The cheaper and more portable a tool, the more likely it will find widespread use, either at a hospital or clinic, or for field use in the developing world.

Beyond the miniaturization of simply the *volume* of the QPCR biological test specimen, this work seeks to provide preliminary documentation on the parallel scaling of the overall dimensions of *instrumentation* needed for QPCR diagnostics.

1.2 Proposed Quantitative Polymerase Chain Reaction Lab-on-chip

The objective of this research is to demonstrate QPCR on nanoliter volume droplets using instrumentation that has been scaled to perfectly match the form factor of the droplet on which QPCR is performed. This work demonstrates a complete QPCR diagnostic test on the surface of a CMOS integrated circuit. The CMOS circuit, designed using a 0.35μm high voltage process, utilizes electrowetting droplet transport as a means of reliably manipulating nanoliter scale droplets on the chip surface. Integrated heaters and temperature sensors, calibrated using a spatially resolved DNA thermometer technique, are used to control the temperature of surface of the lab-on-chip. Geiger mode SPADs are used to monitor the progression of the reaction by measuring the relative fluorescent increase from a laser-excited intercalator dye. *Staphylococcus Aureus (S. aureus)* tests strands are used to test the functionality of the lab-on-chip device.

1.3 Thesis Outline

The thesis outline is as follows: Chapter 2 describes the background on Quantitative Polymerase Chain Reaction, the diagnostic protocol that we sought to integrate on the surface of a CMOS integrated circuit. Chapter 2 goes on to describe the physics behind electrowetting droplet transport. Because a well-regulated temperature on the chip's surface is critical to successful PCR, we also discuss existing methods of temperature sensing considered for use on the chip, highlighting microthermocouples, infrared temperature profilometry, LCD temperature sensing, and concluding with DNA-based temperature

measurement, a method that was modified in this work for the calibration of CMOS-based PCR device. Chapter 3 discusses the design of the PCR chip hardware, focusing on the control circuitry, the embedded heaters and temperature sensors, and the integrated Single Photon Avalanche Diodes. Chapter 4 presents data taken from chip. We demonstrate the successful operation of the chip including droplet transport. Characterization of the heaters, SPADS, and EWOD array is discussed. Results demonstrating a complete 35 cycle qPCR are presented and discussed. Chapter 5 provides the conclusions our qPCR lab-on-chip research, lists the original work of this thesis, and provides future directions in qPCR lab-on-chip devices.

2

Chapter   2:

Application Background

This chapter provides the related principles and implementation methodology of droplet-based PCR. Section 2.1 discusses the chemistry and implementation of PCR and its evolution to qPCR. Section 2.2 explains electrowetting-on-dielectric, the method with which droplets are transported across the chip's surface. Section 2.3 details existing methods of microscale temperature measurements using cholesteric liquid crystals, infrared temperature mapping, and microthermocouples and concludes with an overview of DNA-based temperature sensing, the method used in this work. Finally, an overview of previous work on droplet based PCR instrumentation is given in Section 2.4.

2.1 Quantitative Polymerase Chain Reaction [qPCR]

2.1.1 PCR Mechanics

PCR is a biological protocol in which a specific DNA sequence present in a given genetic test sample can be isolated and set to undergo exponential self-replication [2]. A typical PCR protocol consists of precise thermal cycling of the DNA sample under test in the presence of unbounded nucleotides, the DNA polymerase enzyme, custom primers to isolate the sequence of interest, a florescent intercalator dye for determining the progression of DNA target amplification, and a buffer to maintain constant pH. Each PCR cycle, typically repeated 30-35 times, consists of three steps – denaturation, annealing, and elongation, shown in Figure 2.1.

During denaturation, the DNA is heated beyond the melting temperature of the DNA strands, causing the DNA to transition from a double stranded to single stranded state. Once the strands have fully separated, the temperature is lowered in order to enable the primers to anneal to their binding sites on the newly formed single-stranded nucleotides. The primer sequence essentially places "bookends" around the DNA sequence that is to be isolated and ensures the exponential amplification of that particular sequence. Once the primers have isolated the sequence of interest, the temperature is increased to the optimal operating temperature of DNA polymerase, an enzyme that facilitates complementary base bonding to the single stranded oligonucleotide and allows for double stranded elongation. As this three step thermal cycling protocol is repeated, the DNA template isolated by the primers is exponentially amplified as illustrated in Figure 2.2. Note that PCR amplifies both the target sequence as well as the extraneous DNA segments. A calculation assuming 100%

amplification efficiency is shown in Table 2.1.
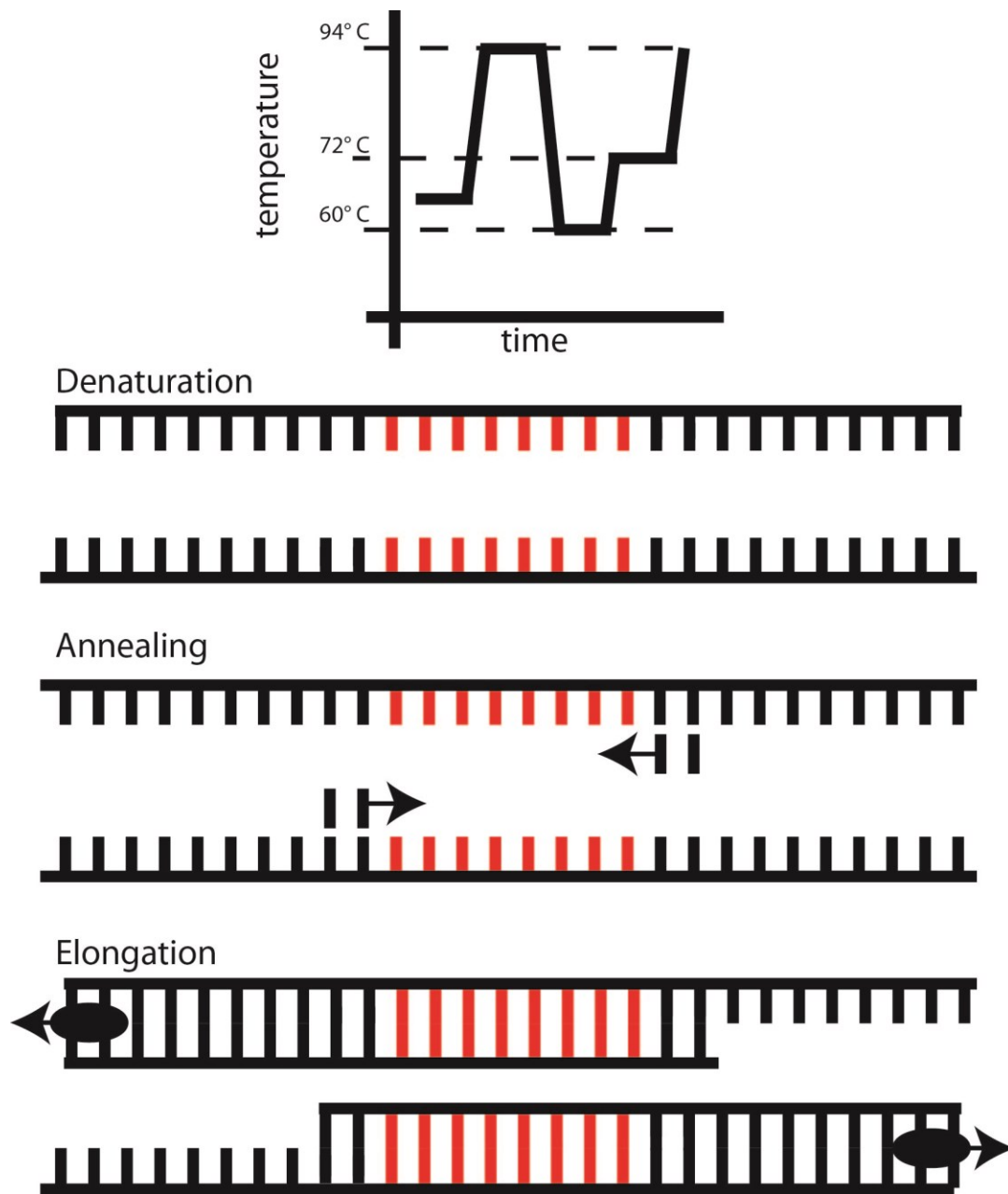
Figure 2-1: Polymerase Chain Reaction cycle #1.

Cycle 2 PCR products
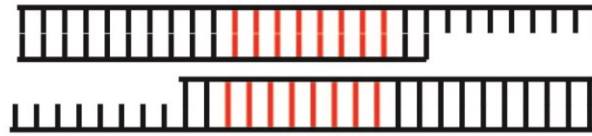
Cycle 3 PCR products
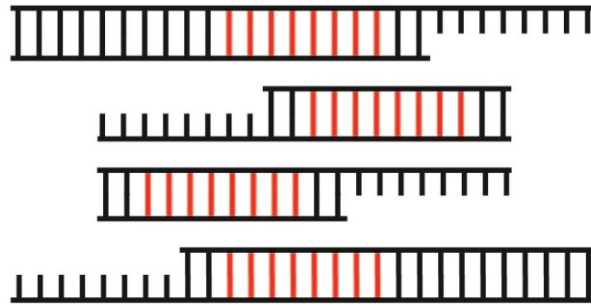
Cycle 4 PCR products
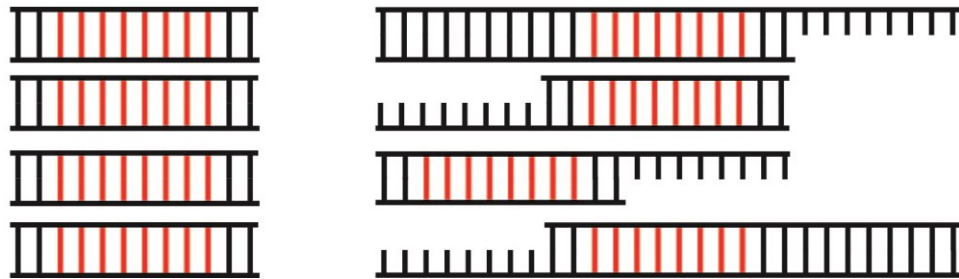
Figure 2-2: PCR cycles #3, #4, #5

PCR cycle	DNA target copies	Total DNA copies
1	0	2
2	0	4
3	2	8
4	8	16
5	22	32
6	54	64
7	114	128
8	240	256
9	494	512
10	1004	1024
15	32738	32768
20	1,048,536	1,104,576
25	33,554,382	33,554,432

Table 2-1: PCR product tabulation

2.1.2   Real-time reaction monitoring using qPCR

In order to monitor the progression of PCR, several methods of florescent microscopy can be employed. Discussed below are TaqMan PCR probes and intercalator dyes.

TaqMan PCR probes [20] [21] are used to monitor the PCR reaction in real-time. The sequence of each TaqMan is engineered so that the probe anneals to within the target DNA sequence that is to be amplified. A fluorophore is covalently attached to the 5'-end of this custom designed oligonucleotide probe and a quencher to the 3'-end. The quencher prevents fluorescent emission when the fluorophore and the quencher are in close proximity.

During each elongation phase, the probe that has annealed to each strand is degraded. Once the probe fully disassembles, the quencher and fluorophore are released

and are thus no longer in close contact. The total florescence due to unquenched probes is proportional to the concentration of degraded probes and thus to the concentration of amplified target DNA oligonucleotides, as shown in Figure 2.3.

primer anneals;
no fluorescence

elongation begins;
no fluorescence

polymerase degrades linker;
fluorescence exists
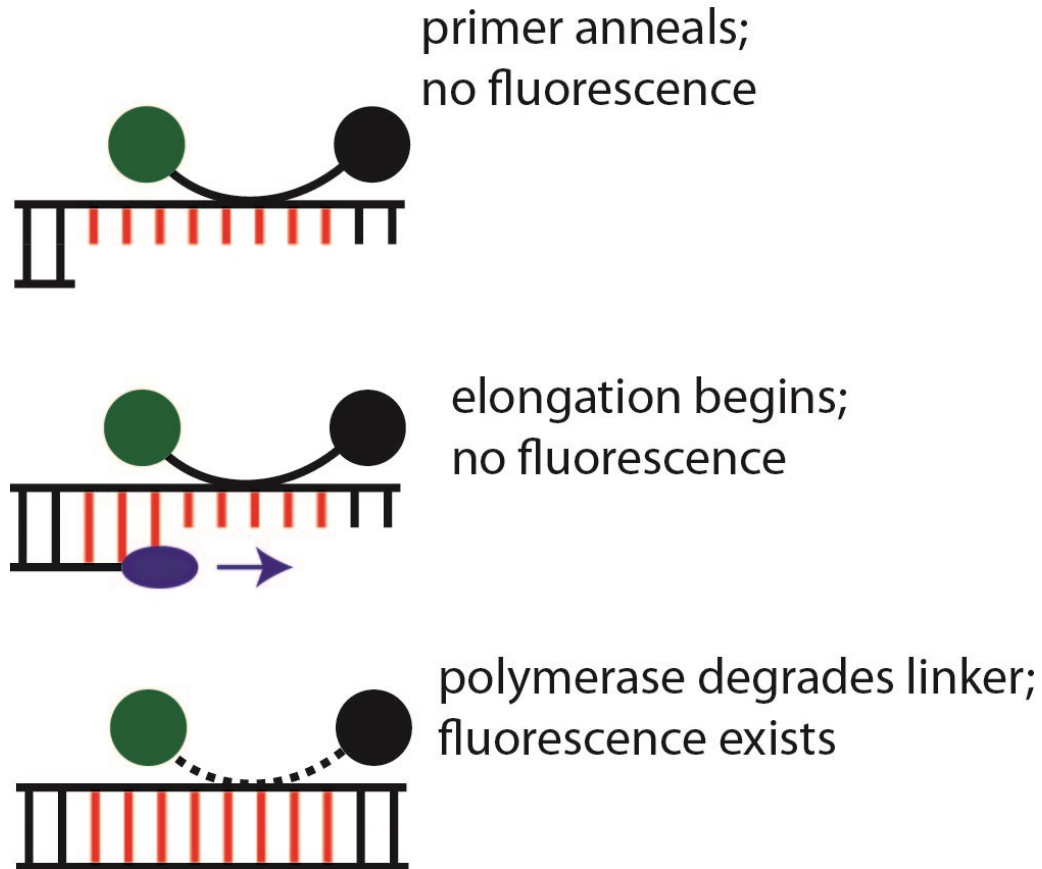
Figure 2-3: TaqMan probe fluorescent tag mechanism

Alternatively, intercalator dyes such SYBR Green I [22] and EvaGreen [23] intercalate between complimentary base pairs of hybridized DNA strands. In the case of EvaGreen, the two monomeric dye molecules are separated by a 19 atom long chain. Due to a combination of mechanical intercalation and electrostatic interaction, the doubled headed dye binds to hybridized DNA strands (Figure 2.4). In a bound state, the EvaGreen dye fluoresces. In the presence of single stranded DNA, the intercalator dye is unable to find its

11

binding site and will not emit fluorescent light when excited. (Excitation/Emission spectra are shown in Figure 2.5.)

Intercalator dyes require less overhead than the quenching and TaqMan dyes. However, the decrease in specificity requires an extra processing step. Intercalator dye fluorescence can increase due to the increased concentration of target DNA sequence as well as from the increased concentration of extraneous DNA strands. In order to differentiate, a DNA melting analysis is performed to verify that the target DNA, whose melting temperature is well known, has in fact been amplified.
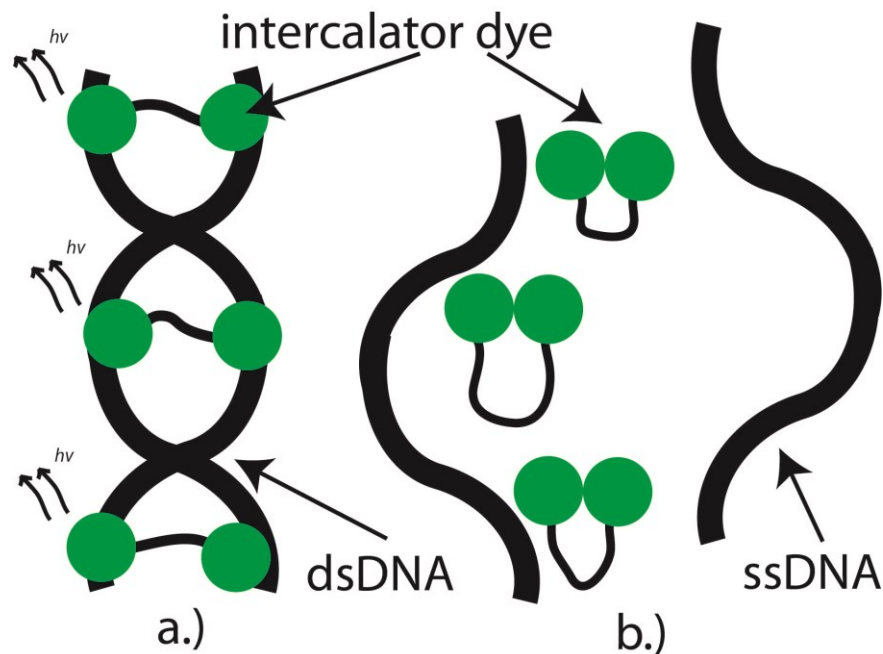
Figure 2-4: Intercalator dye fluorescent mechanism

This work makes use of the EvaGreen intercalator dye for measuring the concentration of the PCR target sequence. During testing, faster experimental turn-around was achieved due to the universality of the intercalator dye. Using the TaqMan setup, though it provides increased specificity, requires the design of custom headers and custom Taqman probes. For any given primer set, real-time PCR monitoring via fluorescent intercalation can be performed using the stock fluorescent intercalator dye, simplifying the reaction setup and reducing the cost per run.
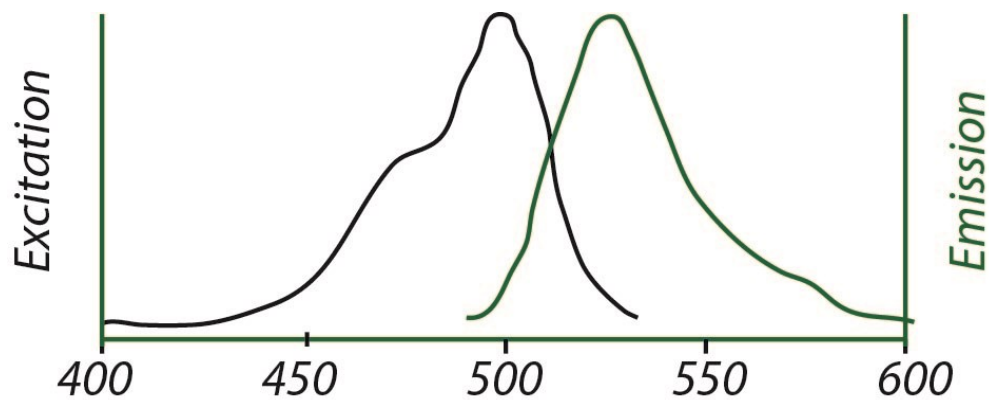
Figure 2-5: EvaGreen intercalator dye excitation/emission spectrum

2.2　Droplet-based Microfluidic Transport

In order to enable QPCR instrumentation scaling to follow scaling improvements in PCR volume per reaction, this work describes the implementation of droplet-based PCR on a CMOS IC using electrowetting on dielectric as a method of droplet transport. Electrowetting-on-dielectric (EWoD) droplet transport provides a means for scaling microfluidics by controlling droplets electrically without the need for external pumps. In the presence of an electric field, a droplet of aqueous regent seeks to minimize its internal energy through translational motion toward the direction of positive voltage.[24-27] Nearly all EWoD devices demonstrated to date are passive, that is, they have no integrated means to control or generate controlling voltages[27-29]. Furthermore, EWoD devices previously employed for QPCR applications have been limited to passive devices with external fluorescence detection[30,31]. The one active CMOS device has been reported was applied to the movement of cells through microfluidic chamber at speeds up to 30 μm sec^{-1}[32] with off-chip detection.

This work seeks to exploit EWoD as a means of achieving a droplet transport scheme on CMOS that perfectly matches both the form factor of the *droplet* being transported as well as the *sensors* that are built into the CMOS platform.

2.2.1　Electrowetting on Dielectric theory

Given a dielectric material in the presence of an AC or DC electric field, electric charges collect at the material interface. As a result, a force is exerted on the interface and can lead to a physical deformation of the dielectric material as shown in Figure 2.6. When the dielectric material is a liquid, this interfacial force is referred to as the electrowetting force.

14
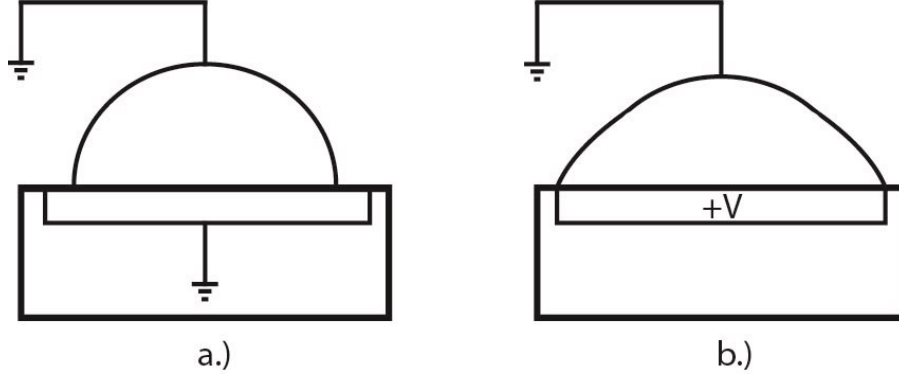
Figure 2-6: Schematic representation of contact angle increase due to applied electric field

The droplet deformation illustrated in Figure 2.6 above is dictated by Equation 2.1, shown below. γ_{LG} is the liquid-gas surface tension, V is the applied voltage, C is the capacitance of the system, dominated by the capacitance between surface and liquid droplet.

$$cos\theta = cos\theta_0 + \frac{C}{2\gamma_{LG}}V^2 \qquad (2.1)$$

Based upon Lippmann's equation, the electrowetting contact angle change is shown to be proportional to the energy injected into the physical system [33-35]. A derivation of this relationship can be obtained through application of energy minimization principles as shown by Shapiro et al. [36,37] in Equation 2.2 where R is the droplet radius, θ is the contact angle, and E is the energy of the system.

$$dE = \frac{\partial E}{\partial R}dR + \frac{\partial E}{\partial \theta}d\theta = 0 \qquad \text{Equation 2.2}$$

Note that R and θ are not independent and are related by the following expression:

$$V(R,\theta) = \frac{\pi}{3}R^3(2 - 3cos\theta + cos^3\theta) \qquad \text{Equation 2.3}$$

By taking the derivative of both sides of the equation and setting dV to zero, dR is given as

follows:

$$dR = R\frac{2cos^2\left(\frac{\theta}{2}\right)cot\left(\frac{\theta}{2}\right)}{2+cos\theta}d\theta \qquad\qquad \text{Equation 2.4}$$

Then, plugging the result into the initial expression for the energy of the droplet/electrode

system, we perform the energy minimization derivation below.

$$\frac{dE}{d\vartheta} = -R\left[\frac{2cos^2\left(\frac{\theta}{2}\right)cot\left(\frac{\theta}{2}\right)}{2+cos\theta}\right]\frac{dE}{dR} + \frac{dE}{d\theta} = 0 \qquad\qquad \text{Equation 2.5}$$

Assuming an ideal dielectric and a uniform electric field, the energy stored in the dielectric is

given as

$$E_{EWOD}(R,\theta) = \frac{\varepsilon_0\varepsilon_D V^2}{2d}\pi R^2 sin^2\theta \qquad\qquad \text{Equation 2.6}$$

The total electric energy of the system is the difference between the energy that is stored in

the dielectric and the energy from the external charging supply, which is twice the amount of

energy in the dielectric. When the droplet's contact angle changes due to the influence of

the applied electric field, a packet of charge ΔQ much be received from or pushed back

against the voltage source. Since $W = V\Delta Q$, the energy stored in the charge supply is then

twice the energy sored in the dielectric. Total energy is then given as

$$E = R^2\left[\left(\gamma_{SL} - \gamma_{SG} - \frac{\varepsilon_0\varepsilon_D V^2}{2d}\right)\pi sin^2\theta + \gamma_{LG}2\pi(1 - cos\theta)\right] \qquad \text{Equation 2.7}$$

$$cos\theta = cos\theta_0 + \frac{\varepsilon_0\varepsilon_D V^2}{2\gamma_{LG}d} \qquad\qquad \text{Equation 2.8}$$

This result forms the core of the droplet transport scheme utilized in this work. In going

through the mathematical rigor, Equation 2.1 has been derived using an energy minimization

approach.

In mechanical terms, this result describes the nature of the droplet movement under

the influence of an applied electric field. Considering the resultant of the electric force on the liquid gas interface, the electric field and thus total charge concentrate at the edges of the droplet and produces a finite Maxwell force at the contact line. Because the aqueous droplet has a higher permittivity and a higher conductivity than the surrounding medium, a force is generated and leads to the mechanical deformation of the droplet [14]. These principles of the mechanical deformation of a aqueous droplet have been applied to induce droplet transport across a programmable electrode array.

2.2.2 Droplet Transport using Electrowetting

Given a droplet located on the boundary between a nominally hydrophobic region and a comparatively hydrophilic region, Teflon AF and untreated glass for example, the liquid droplet will move or conformally distort in an attempt to move to the hydrophilic region, so long as the hysteresis of contact angle is not too large. Similar transport phenomenon is observed in the case of electrowetting in which electric fields are applied to induce changes in surface wettability. When the conductive droplet is located on the boundary between an actuated (hydrophilic) and a grounded (hydrophobic) electrode, an electrowetting force is applied to the contact line between the droplet and the electrode, and a capillary force is exerted on the contact line. The resultant of the forces parallel to the surface is directed towards the electrically actuated region. Given these electrostatically induced forces, the droplet moves in order to come to an equilibrium state assuming the induced force can overcome contact angle hysteresis. The principle of droplet motion is thus due to a wettability gradient that is electrostatically induced.

The device developed in this work utilizes the electrowetting effect as a means of

electrostatically transporting droplets across a two-dimensional array. The core architecture this transport mechanism involves microscale (200μm x 200μm) electrodes embedded within a solid substrate - in the case of this work, a CMOS silicon die. The dimensions of each electrode roughly correspond to the nominal size of each droplet. The electrode array is conformably coated with a dielectric layer (Parylene C) covered by a hydrophobic layer (Teflon AF) in order to increase the electrowetting effect on the droplet.

Digitally controlled actuation of pixel electrodes is used to set the path of a given droplet. Droplets are initially generated from a droplet dispenser, typically much larger in size than the other pixels. Individual droplets that have entered the electrowetting array can be moved between adjacent electrodes[26], merged with other droplets, and thoroughly mixed [25,28] , depending upon the particular biological reaction that is to be conducted using the device. Once the reaction is complete, the droplet is moved to a section of the chip designated for waste products and can be removed via syringe or automated vacuum. The advantages of such devices are the use of lower quantities of costly reagents, better biochemical reaction efficiency, and shorter operating times.

In designing the integrated circuit capable of droplet transport, it is of value to determine the minimum voltage needed to transport a droplet of a given volume and radius. Typically, several factors must be considered in this analysis, such as contact angle hysteresis, drag from the filler fluid (n-dodecane), drag from device side walls, and change in applied force when the device is moving. The following equation (2.9) simplifies these factors as it focuses on the effect of the filler medium. The minimum actuation voltage, V_T, is then given as follows:

$$V_T \approx \sqrt{\frac{2t\gamma_{LG}}{\varepsilon_o\varepsilon_o}}$$
Equation 2.9

In order to estimate the surface tension of the droplet, we refer to Richard Tolman's work[38] on determining the relationship between droplet dimensions and the resultant surface tension. As seen the table below, for large droplets, droplets whose radium of curvature is much greater than the surface of tension to the dividing surface, little change in effective surface tension is observed. However, as the radius of curvature is decreased, significant decrease in the surface tension is measured. This relationship is tabulated below in Table 2.2.

δ/r	γ/γ_0
0	1
0.01	0.98
0.02	0.96
0.05	0.91
0.1	0.83
0.2	0.70
0.3	0.60
0.4	0.52
0.5	0.46
0.6	0.41
0.7	0.36
0.8	0.33
0.9	0.30
1	0.28

Table 2.2: Effect of droplet scaling on surface tension

Assuming a thickness of dielectric material Parylene C of 2μm with a relative dielectric constant of 3.15, the device that we need to design requires an actuation voltage of approximately 90V.

Having determined the actuation voltage for the electrowetting system, it is of interest to determine the speed at which these droplets are capable of moving on the surface of the device. In this digital microfluidic system, a droplet moves from pixel to pixel. Given the incremental nature of the transport and the time constant of the electrowetting charge injection event, the droplet accelerates quickly, reaches its near steady-state velocity, and abruptly decelerates. The near-steady state velocity of a given droplet is approximated below.

$$v_{droplet} \approx \frac{\delta}{12\pi\mu r} CV^2 \qquad\qquad \text{Equation 2.10}$$

The derivation assumes that the electrowetting force balances the friction force due to viscous dissipation at the boundary of the droplet and the surrounding medium. Note that since a hydrophobic surface is used, the friction force from the droplet substrate boundary is negligible.
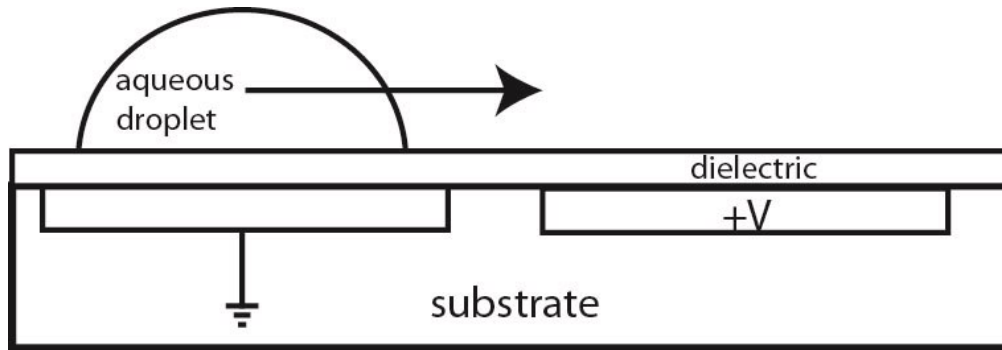
a.)
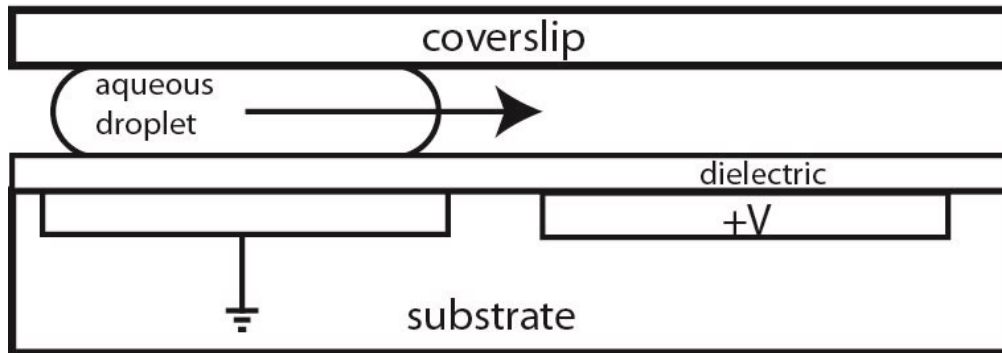
b.)

Figure 2-7: Schematic representations of open and closed EWOD configurations

Two electrowetting configurations were considered for implementation (Figure 2.7). Using an open electrowetting device, one electrode is held at the actuating potential while the other electrode is tied to ground. Note that the potential of the droplet is floating. In a covered EWOD system, a grounded top plate is introduced to cover the droplet. The surface area between liquid and surrounding medium is significantly reduced in this design. Complications related to evaporation are avoided. Given that a greater fraction of the

droplet is subjected to stronger electric fields, a lower actuation voltage can be used given a certain droplet diameter moving a given saturation velocity.

2.3 Methods for microscale temperature measurements

As discussed in Chapter 2.1, maintaining stable and precise temperature control on the PCR test solution is critical. Slight temperature fluctuations during the elongation stage can lead to incomplete complementary base pair bonding. In order to calibrate the miniaturized temperature control instrumentation demonstrated in this work, a custom calibration tool was developed. Sections 2.3.1 and 2.3.2 discuss infrared temperature mapping and microthermocouples which were considered in this work but not used. Section 2.3.3 details previous work done on using a DNA and its particular melting curve as the sensing element of a thermometer that formed the basis for temperature calibration on temperature sensors used regulate the surface temperature of the lab-on-chip qPCR tool.

2.3.1 Infrared Temperature mapping

Mercury telluride or cadmium telluride single-element infrared (IR) arrayed detectors were considered as a possible means of determining the IC surface temperature in order to calibrate the temperature sensors that are located in metal layer 3 (second layer from the top in a 4 metal stack) of the lab-on-chip. However, due to the complications from surface emissivity compensation and obtaining a baseline room temperature reading, IR temperature mapping was not used for this chip.

2.3.2 Microthermocouples

Microthermocouples were considered as means of obtaining precise temperature measurements on the surface of the device. Thin film Cr–Ti microthermocouples have previously demonstrated in literature. [39] The dimensions of this particular device are as follows: Width of tip: 200μm, length of legs: 10,100μm. However, due to the size of these devices, the thermal load they would present, and the post-processing complications of integrating them practically with the electrowetting array, microthermocouples were not used in this work.

2.3.3 DNA melting curve temperature measurement

The methods described in the previous section all present a finite thermal load to the surface whose temperature is to be measured. To obtain an ideal calibration, the temperature sensing element should present the same thermal load as will be present during the actual use of the device. The authors Tashiro[40] and Jeon[41] have presented methods to measure temperature using the fluorescence lifetime of fluorescent-labeled DNA oligonucleotides. In this case, the temperature sensing element is an aqueous solution of nearly identical composition to the composition of the droplets during an actual run of qPCR on the device.

The method described in literature is as follows [41] : an excitation volume of 15 μL is excited with a focused laser. DNA bases quench fluorescence with variable efficiency. Thus, the spacing between a fluorescent dye and a custom-designed DNA sequence is dictated by the conformational changes of the DNA chain. The ability of dye molecules to fluoresce is also thus also a function of temperature. As temperature increases, the rate of conformational changes increases and the fluorescent lifetime decreases. By measuring the

fluorescent lifetime, a precise measurement of temperature can be determined. More specifically, this method was demonstrated using rhodamine-labeled DNA oligomer, 5'-RhG-GATGATGAGAAGAAC-3', in which the rhodamine-G dye was separated from the main chain by a sequence of 6 methylene units. In this specific example, two-photon excitation by a femtosecond Ti:Sapphire laser. The DNA concentration in solution was ~2 μM. This method is noninvasive. However, its primary shortcoming is that it has only been demonstrated on microliter volumes. Although previous literature only demonstrates the use of a very specific DNA oligonucleotide, the method can be generalized to a wide selection of sequences, each with their melting and conformational properties.

In this work, the idea of using DNA as a temperature sensitive element is modified and extended for use as a means of obtaining a spatially resolved temperature mapping. Instead of using a large volume of the DNA-based temperature sensitive element as a means of obtaining a single temperature reading, the volume is decreased and the geometry reduced to a thin-film form factor. The primary sensing mechanism is no longer the florescence lifetime as modulated by conformational changes. Rather, the fluorescent intensity of an intercalator dye modulated by the state of DNA melting is used a gauge of temperature. Although photobleaching must be considered and compensation parameters carefully measured, the ease of designing oligonucleotide with specific melting properties makes this an indispensable tool for precise temperature measurements. The method of obtaining spatially resolved temperature measurements using DNA melting curve thermometer is described in greater detail in Chapter 3.

Before considering the use of DNA as the method of obtaining a spatially resolved

temperature mapping for calibration purposes, cholesteric liquid crystals were considered. Cholesteric liquid crystals, derivatives of cholesterol, have liquid-like properties and thus would present a similar thermal load to the surface of the lab-on-chip device. [42,43] Furthermore, over a controllable temperature range, the optical properties of the liquid crystal are modulated, leading to a measurable color change. The temperature range can be as tight as 0.5 ºK or as wide as 50 ºK. Measurement would require illumination by white light in order to measure the precise wavelength that the liquid crystal reflects at a given temperature; this occurs by virtue of their molecular structure at a given temperature and the change of structure with temperature. The reaction is reversible. Output varies from red at low temperatures and violet at high temperatures. Response time is on the order of hundreds of milliseconds. High resolution spatial mappings can be obtained, limited by the quality of the optics used to image to liquid crystal film. This method was considered and ultimately proved a model for the DNA thermometer described in Chapter 3. However, the need to take LCD image readings with a perfect black base would have required post-processing that would be incompatible with the implementation of the hydrophobic surface treatments needed to implement electrowetting on dielectric droplet transport on the lab-on-chip device. The DNA thermometer method, although requiring much rigor in obtaining calibration curves for the DNA temperature sensing solution, proved the most flexible approach due to the ease of designing temperature specific solutions.

2.4 Previously demonstrated micro-PCR devices

Many examples of microscale PCR devices have been described in literature. These include

but are not limited to the following: A PCR based plasmid purification system[44], a PDMS / glass hybrid device that performed continuous flow PCR[45], a nanoliter droplet based device capable of performing 40 cycles in less than six minutes[46], continuous flow PCR device built on polymethyl methacrylate[47], a device that utilizes capillary driven sample loading[48], an microscale PCR lab-on-chip for detection of avian viral influenza lab [49], a PDMS based PCR device with Parylene coating[50] , a nanoliter droplet array for rt-pcr[50]. The device presented in this work builds upon the work of past PCR devices but seeks to push the boundaries of PCR devices, namely in terms of the scaling of the device's form factor.

Thus far, the dimensions of the lab-on-a-chip systems and the volumes of reagent which undergo QPCR demonstrated in literature have been much smaller than those of commercial QPCR machine. [51] [52] However, size reductions of the complete unit including instrumentation have not scaled as radically as the droplet upon which QPCR operates. Most demonstrated lab-on-chip units use commercially available fluorescence detectors and thermal cyclers. Cumbersome instrumentation prevents further downsizing of QPCR chips. This work integrates the thermal cycling control loop and fluorescence detection circuitry into the lab-on-chip device, allowing device scaling in line with reagent scaling.

Complementary metal-oxide-semiconductor (CMOS) integrated circuit (IC) technology provides a unique opportunity to further scale PCR hardware by providing for high-bandwidth, distributed temperature control across the chip surfaces and integrated detection. Tomazou et al. [53] describe the first CMOS-based qPCR IC. Instead of using fluorescence detection, pH is monitored during PCR to gauge the progression of the reaction with heating and temperature control also performed on-chip[53]. This device is still

limited by use of microfluidic pumps, requiring reagent volume on the microliter scale. Sensitivity is limited by noise in the integrated ion-sensitive field-effect transistors to 10 copies per sample.

The advantages of QPCR on a CMOS chip are the extreme low sample volume consumption and short analysis time for DNA quantification. Using microstructures and miniature chips, the PCR sample volume consumption of a chip is reduced almost one thousand times from that of bench-top machines. Due to the reduced thermal capacity of nanoliter droplets, the reagent is able to reach is able to reach thermal equilibrium much more quickly. The time constant required for temperature stabilization can be reduced from 15 to 40 seconds required in commercial units to less than 1 second.[46] However, one major bottleneck that prevents further reduction in total QPCR duration is the rate at which the Taq polymerase operates upon the droplet. Although the droplet itself is able to reach thermal equilibrium much more quickly than in 25-50µL volumes, the length of the elongation stage is still dictate by the length of the DNA target and the speed of the Taq polymerase, which is typically less than 10 base-pair unions per second.

Previously demonstrated devices have yielded poor detection limits. Again, this stems from the fundamental mismatch of the droplet to its instrumentation. Nanoliter droplets with fluorescent intensities more than 1000 times smaller than their microliter counterparts prove a challenge to commercially available photodetectors.

Given the decreased fluorescent outputs and low sensitivities of instrumentation, the reproducibility of QPCR amplified target quantification with a single chip is not as good as that of tests performed using a commercially available machine. Temperature variation

across the chip also accounts for the large variation across measurements. Typical accuracies of the chip prototypes range from ±0.2ºC to ±0.5ºC which is sufficient for PCR applications. However, non-uniformity across the lab-on-chip structure ranges from 0.5 to 5ºC. A commercially available machine with a large metal heating block can provide temperature variation as low as 0.01ºC across the 96 well plate. In addition to the temperature variation across the lab-on-chip surface, it is important to note the potential role of surface inhibition effects. Due to the increased surface-to-volume ratio present in nanoliter droplets, surface adsorption phenomena occur and QPCR amplifications can be notably inhibited. Thus, both the temperature non-uniformity and inhibition effects lead to variation in the quantification of QPCR products.

The QPCR device demonstrated in this work seeks to document the effectiveness of full integration of QPCR actuation and sensing onto a single CMOS lab-on-chip platform. Unlike the devices discussed above, the device designed as part of this work matches the instrumentation to the form factor of the nanoliter droplet of QPCR reagent. However, due to the close proximity of the droplet actuation, photodetection, and heating components, careful characterization- namely across temperature- must be performed to determine and compensate the effects that the integrated devices have on one another (Chapter 4).

Chapter 3:

Design of a Polymerase Chain Reaction Lab-on-chip with electrowetting-based droplet transport

This chapter describes the design and implementation of a microfluidic device that performs the Quantitative Polymerase Chain Reaction on the surface of a CMOS integrated circuit. The chip contains an electrowetting-on-dielectric electrode array, integrated heaters and temperature sensors for thermal control, and single photon avalanche diodes for fluorescence sensing.

Section 3.1 provides the details for the electrowetting droplet transport array from the block level architecture down to individual electrowetting control pixel circuitry. Design choices for the heaters and temperature sensors are discussed in Section 3.2. The design of the single photon avalanche diodes that are used for fluorescence detection are explained in Section 3.3. Finally, post-processing and chip packaging/encapsulation techniques are detailed in Section 3.4.

3.1 Electrowetting-based Droplet transport control Circuitry

The electrowetting control array consists of a 7x8 array of 200um x 200um pixels, shown below in Figure 3.1. Four additional droplet generators each consisting of non-regular pixel geometries are included. Each pixel contains active circuitry for storing the state of each pixel. A special level shifter is used to apply the high voltage EWOD actuating potential. Handshake circuitry ensures error free data loading for correct electrowetting droplet placement.
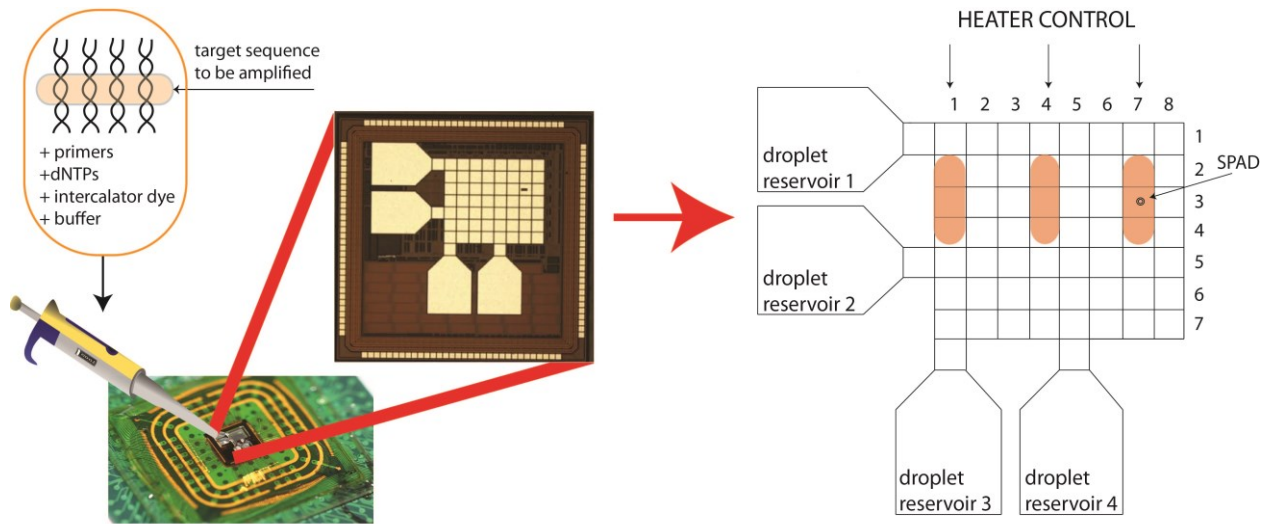
Figure 3-1: PCR chip device overview

3.1.1 Charge pump design

An on-chip Dickson charge pump that steps up the voltage from 3.3V DC to the required 90V DC needed for electrowetting was attempted on the chip. Typically, each stage of a Dickson charge pump consists of a diode connected transistor and a capacitor, shown below in Figure 3.2 [54,55]. Functionality of this component is as follows: Assuming φ_1 is initially low and φ_2 is initially high, current will flow through capacitor C_1 until node V_1 reaches V_{IN}-V_T. When the clock switches, φ_1 goes high and φ_2 goes low. Because the voltage dropped across a capacitor cannot change instantaneously, node V_1 increases to $V_{PHI} + V_{IN} - V_T$. Node V_2 then charges to $V_{PHI} + V_{IN} - V_T - V_T$. Extending the derivation to the Nth voltage node, we see that the charge pump output voltage is as follows:

$$V_{OUT} = V_{IN} + N(V_\varphi - V_T) - V_T \qquad \text{Equation 3.1}$$

If we account for the effect of stray capacitance on the output voltage of the charge pump, the decreased value is given as

$$V_{OUT} = V_{IN} + N\frac{C_1}{C_1+C_S}(V_\varphi - V_T) - V_T \qquad \text{Equation 3.2}$$
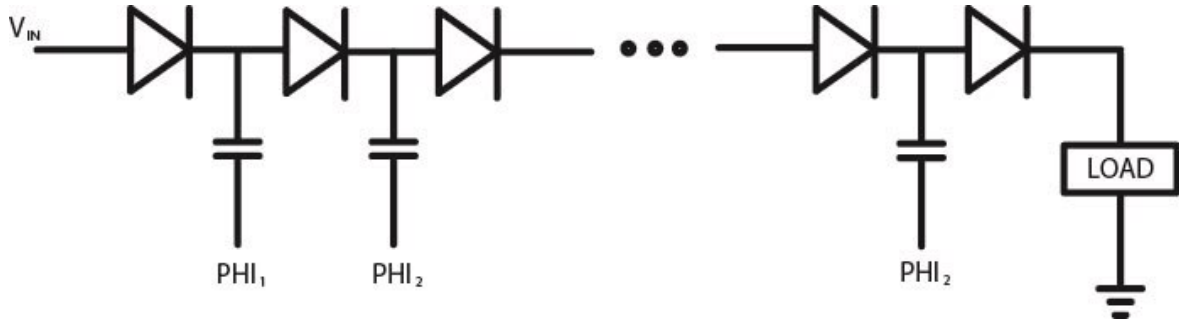
Figure 3-2: Dickson Charge pump using diode connected transistor unit cell

High voltage devices have successfully been demonstrated CMOS substrates using the Dickson Charge Pump configuration using diode connected transistors. [56] [57] The simplest configuration for use on the PCR chip would have been to implement diode connected NMOS transistors with their bulk connections tied to ground. Such devices have been demonstrated in literature, but have not required many stages due to significantly lower output voltages (15V – 25V) than required in this work. The benefits to such a configuration besides simplicity and low transistor count is that no matter what the state of conduction of the diode connected transistor (ON or OFF), the implicit drain-body diode will not turn on and will always be reverse biased. The problem with this design is the body effect and the resultant increase in the V_T of the diode devices as higher order nodes of the

chain. However, since the output voltage of the charge pump as given by Equation 3.2 is strongly dependent on the transistor threshold voltage, the increase in V_T significantly lowers the charge pump output voltage for a given number of stages, N.

A modified configuration considered for use in the work was the use of the implicit drain-body diode as the Dickson diode device. However, this connection scheme greatly increased the parasitic capacitance at each stage, again decreasing the overall gain of the device since some of the capacitively coupled clock voltage would be wasted as it is dropped across this parasitic capacitance.

The solution presented in this work relies upon the selective toggling the body voltage. When $V_D > V_S$, the bulk is tied to the source to minimize the body effect. When $V_D < V_S$, the body is tied to the drain to prevent current leakage through the implicit body drain diode.

Thus, our charge pump design opts for a three transistor based unit cell, inspired by Shin et al [58]. The charge pump schematic is given in Figure 3.4 and corresponding component sizing are provided in Table 3.1. Device operation is as follows: M_{C2} turns on when the diode-connected transistor M_{C3} is not conducting forward current. Since the drain and body are tied together, current does not flow through the transistors intrinsic drain-body diode. By preventing the flow of this parasitic current, we increase the efficiency of the device. Transistor M_{C1} turns on when the diode connected transistor is forward biased. Since the body and source of the diode connected transistor M_{C3} are joined together through M_{C1}, voltage output degradation caused by the body effect is mitigated. The unloaded voltage waveforms at successive nodes along the charge pump are shown Figure 3.3. The device, with no active loading, is capable of pumping up to 103 V with a ripple of 4.7 V.
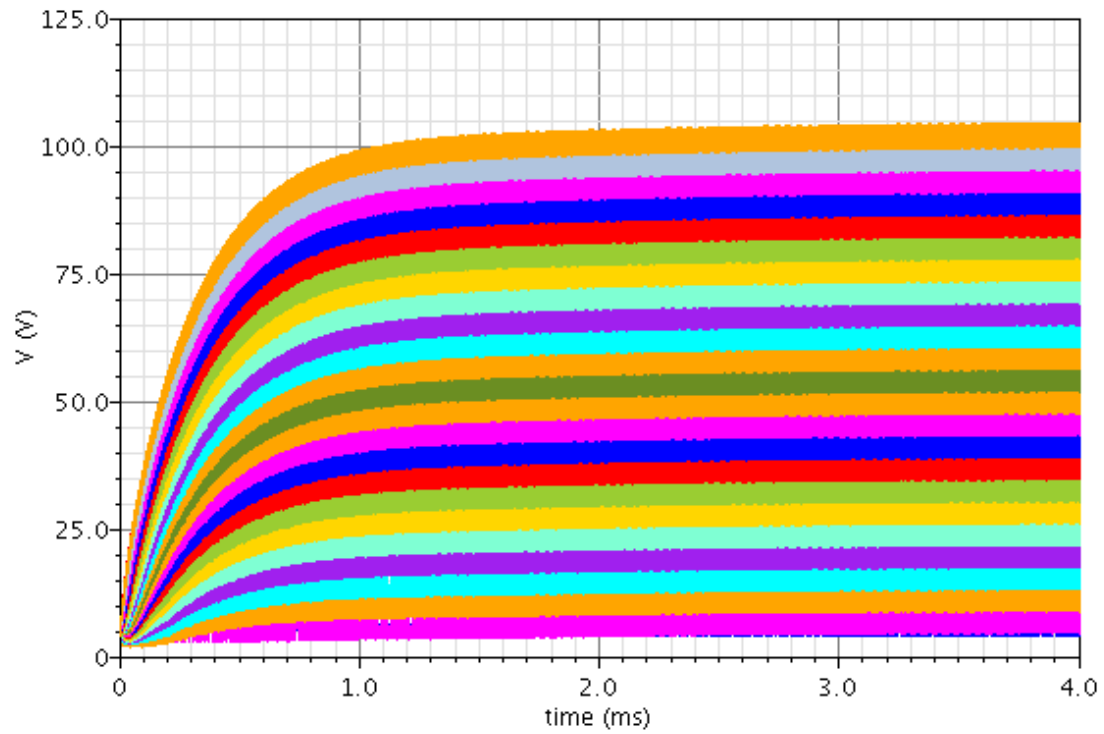
Figure 3-3: Simulated charge pump waveforms

Despite the careful design of the charge pump, reliability issues pertaining to the charge pump capacitors led to on-chip high voltage failure in 35% of our devices. On these select devices, 90V was brought in from off-chip using a bypass.

Charge Pump Component	Sizing
M_{C1}	W/L = 20μm/1.2μm
M_{C2}	W/L = 20μm/1.2μm
M_{C3}	W/L = 20μm/1.2μm
C_1	374μ x 144μm

Table 3-1: Component sizing for modified Dickson Charge Pump using 3-transistor unit cell

Figure 3-4: Modified Dickson Charge Pump using 3-transistor unit cell circuit schematic

3.1.2 Level Shifter design

Each 200μum x 200μm pixel contains a dedicated flip-flop memory cell and high voltage level shifter that allows 3.3V logic to control the 90V electrowetting actuation voltage, shown in Figure 3.5. The level shifter makes use of high voltage transistors that ensure that drain-bulk breakdown does not occur. Furthermore, the use of cascode transistors M_{I2} and

M_{R2} in conjunction with their biasing voltage prevents the breakdown of the gate dielectrics of transistors M_{L3} and M_{R3}. The sizing of the level shifter transistors is given in Table 3.2 below.

Level	W/L
M_{L1}	20μm / 0.5 μm
M_{L2}	10 μm / 1.2 μm
M_{L3}	10 μm / 10 μm
M_{R1}	20 μm / 0.5 μm
M_{R2}	10 μm / 1.2 μm
M_{R3}	10 μm / 10 μm
M_{O2}	10 μm / 10 μm
M_{O1}	20 μm / 0.5 μm

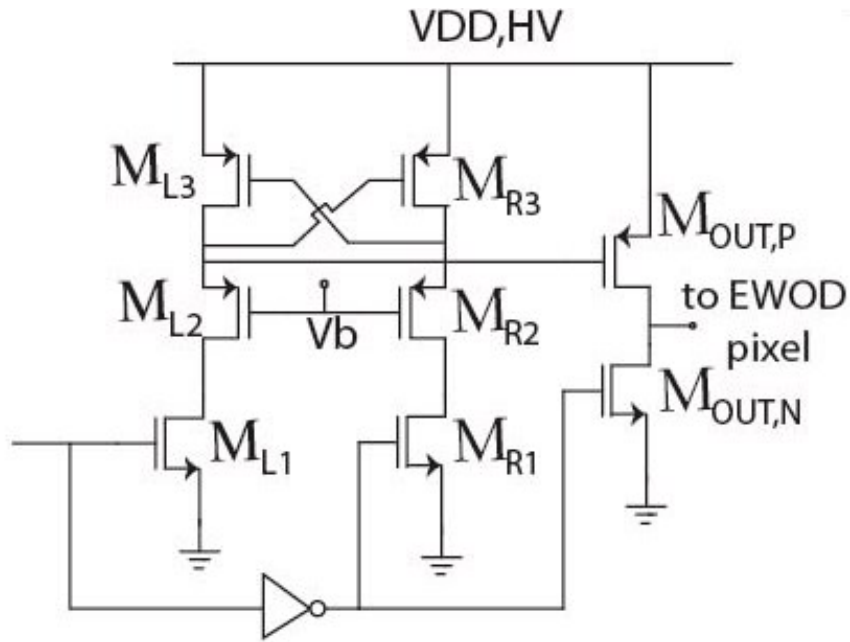Table 3-2: High voltage level shifter transistor sizing

Figure 3-5: High voltage level shifter circuit schematic

3.1.3 Droplet Transport Control logic

The integration of sensors and actuators onto the lab-on-chip device allows us to perform precise heating and temperature sensing at the micron scale. Existing flow based microfluidics, however, do not take full advantage of the small scale heating that can be facilitated by a CMOS microchip. In order to minimize the volume of reagent consumed per QPCR analysis, droplet-based analysis is performed on the device. A pixel dimension of 200μm x 200μm allows for a droplet size of approximately 1.2 nanoliters on our covered electrowetting array. By using electrowetting droplet transport, we avoid the use of bulky pressure-based microfluidic controllers and thus improve device portability.

The primary electrowetting control circuitry is shown in Figure 3.6. Eight electrowetting droplet control bits are loaded in parallel. Synchronization circuitry ensures that the bits have been received prior to clocking the bits into the array. A 3-bit address signal is decoded to determine which of the 8 rows is updated. The state of each pixel is held by a D-latch whose output is connected to a specially designed HV level shifter. The chip moves droplets by completing a row-by-row rewrite at 100Hz. Handshake circuitry (Figure 3.7) ensures data synchronization. The complete data loading sequence of the logic is as follows:

Data is placed onto the 8-bit data bus. The address is loaded on to the 3-bit address bus. The 8-bit request signal is toggled to indicate that the data is ready. Operation of the circuitry is as follows: Assuming that the request signal is toggled from low to high, Node A is taken from low to high. Node B then flips from low to high, and node C goes from low to high. Continuing along the handshake signal path, node D goes from low to high after

being clocked. At this point, the request trigger goes from low to high. This action leads to two events. The 8-bit data is passed to the Data_ready node. The Req_trigger also causes the 8-bit acknowledge bus to toggle. ACK signals are passed to the on-board processing. When all eight acknowledge toggle events are detected, the on-board microcontroller sends the acknowledge_all signal, indicating that the chip has successfully received all of the data bits. As a result of receiving the acknowledge_all signal, 8 bits of data to pass from the data_ready node into the individual latches of each electrowetting pixel. Fully loaded circuit configuration (Figure 3.9) is capable of supplying an electrowetting driving voltage as shown in Figure 3.8.
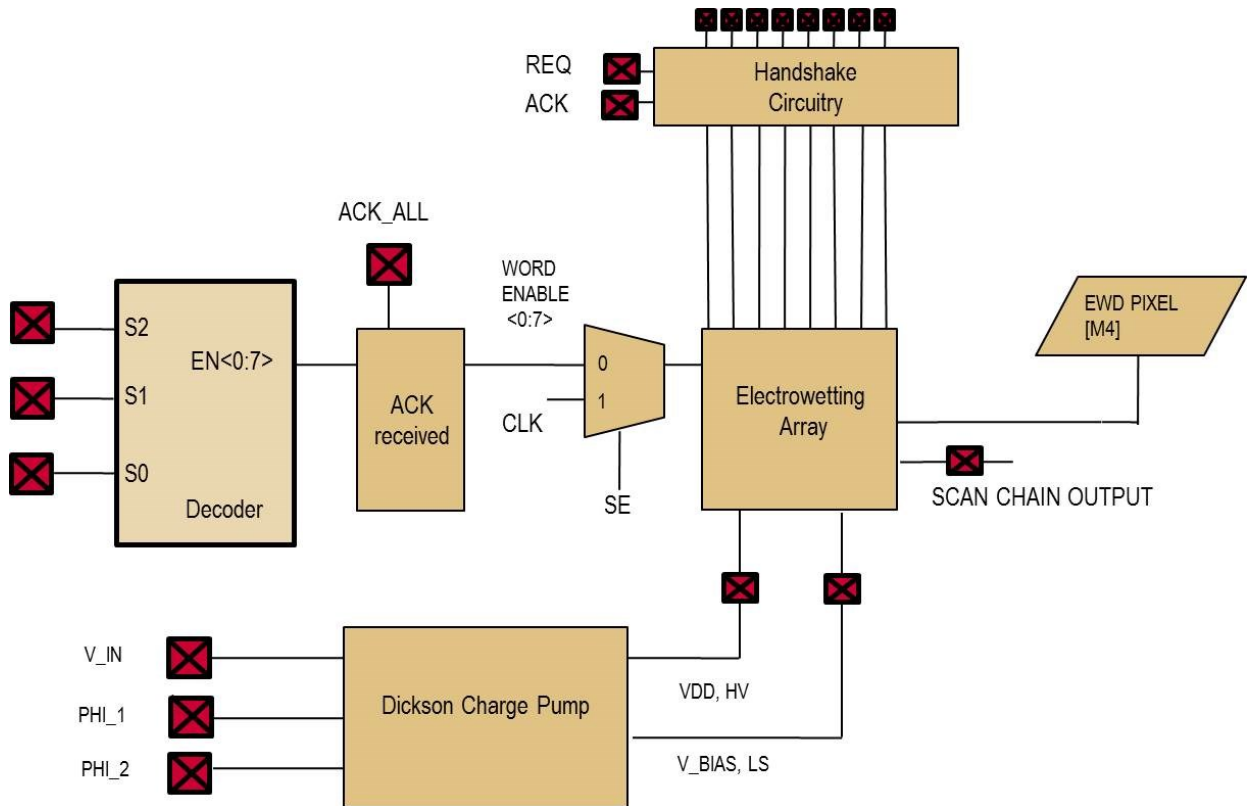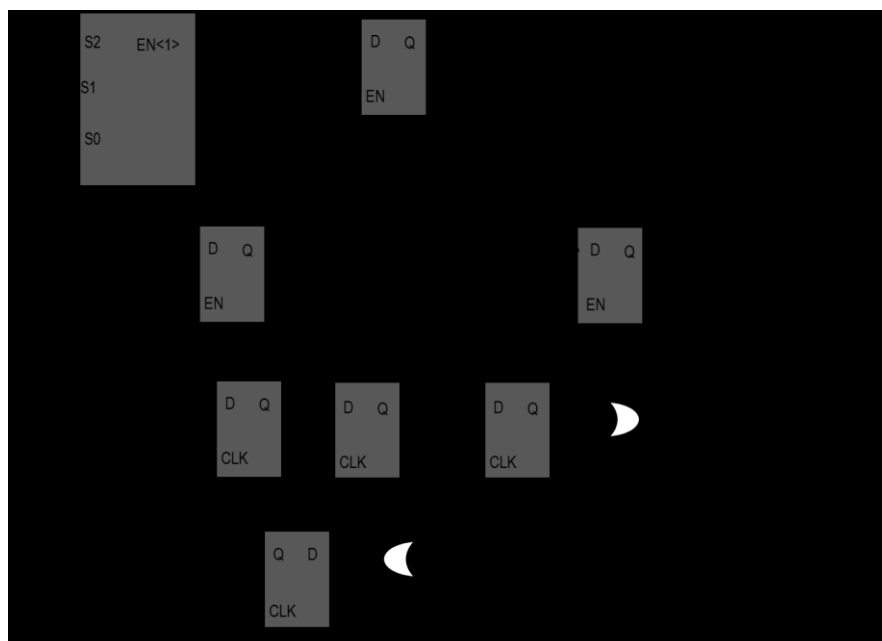

Figure 3-6: PCR chip operational overview

38
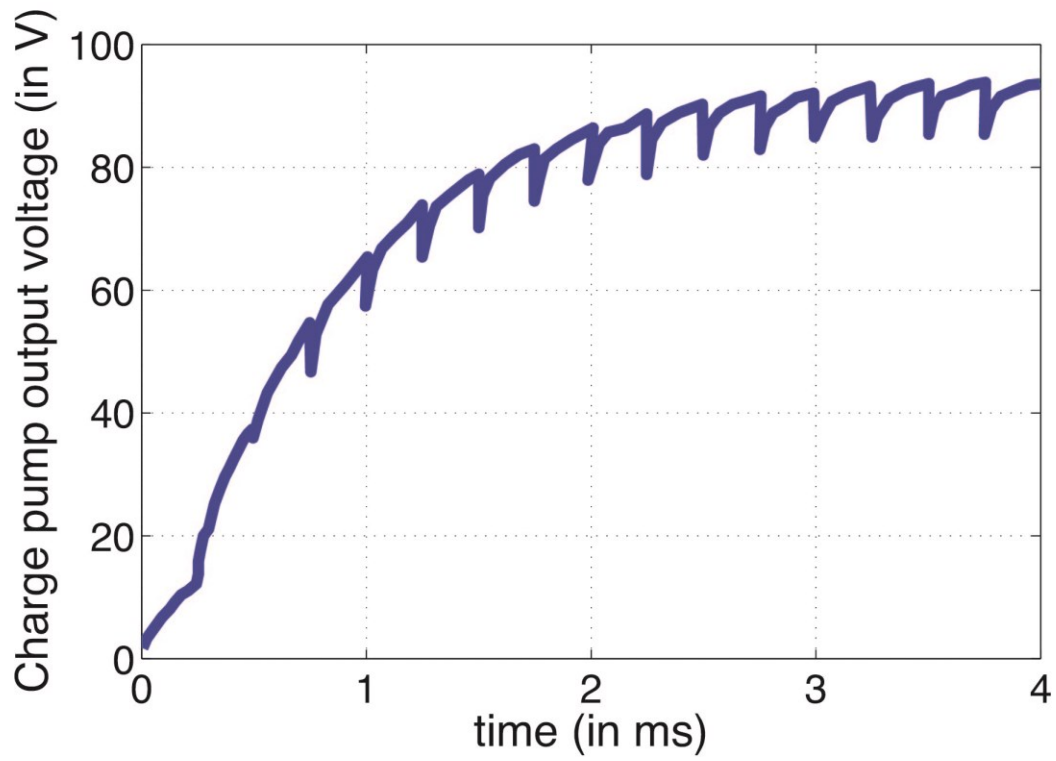
Figure 3-7: On-chip Handshaking circuitry

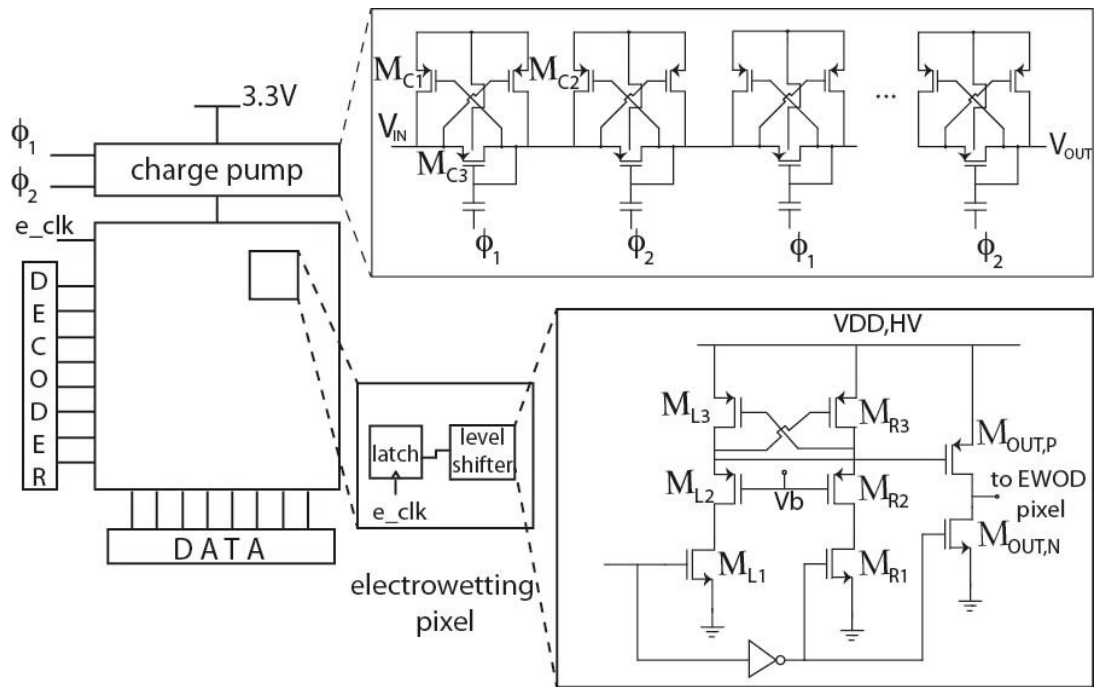Figure 3-8: Fully loaded charge pump output voltage

Figure 3-9: PCR-chip circuitry

3.2 On-chip heaters and temperature sensors

Temperature control is maintained on the surface of the chip with on-chip sensors and heaters. Current is passed through high-resistance polysilicon resistors to heat the chip. Resistive temperature sensors consisting of serpentine interconnect metal are calibrated to monitor the temperature.

Placement, material selection, and sizing of the resistive heaters were optimized through COMSOL finite element mesh modeling simulations. Initial calculations were performed using the constants given below and one-dimensional heat flow analysis. Figure 3.10 was converted into a series of thermal resistances. Equation 3.3 was applied to the resulting network of series connected thermal resistances and used to determine the minimum heat flow injected into the system from the polysilicon heater layer to induce a temperature of 94°C at the surface of the structure.

$$\frac{d}{dx}\left(k\cdot\frac{dT}{dx}\right) + q = \rho c_p \frac{dT}{dt}$$

Equation 3.3

Material	Thermal Conductivity [W/(m*K]	Specific heat [J/(kg*K)]	Density [kg/m^3]	Thermal diffusivity [(m^2)/s]
aluminum	250	900	2700	0.000102
Silicon Dioxide	1	740	2197	6.15e-7
Parylene C	0.0837	720	1289	9.01e-8
n-dodecane	0.135	2186	750	8.23e-8
Water	0.58	4185	1000	1.38e-7

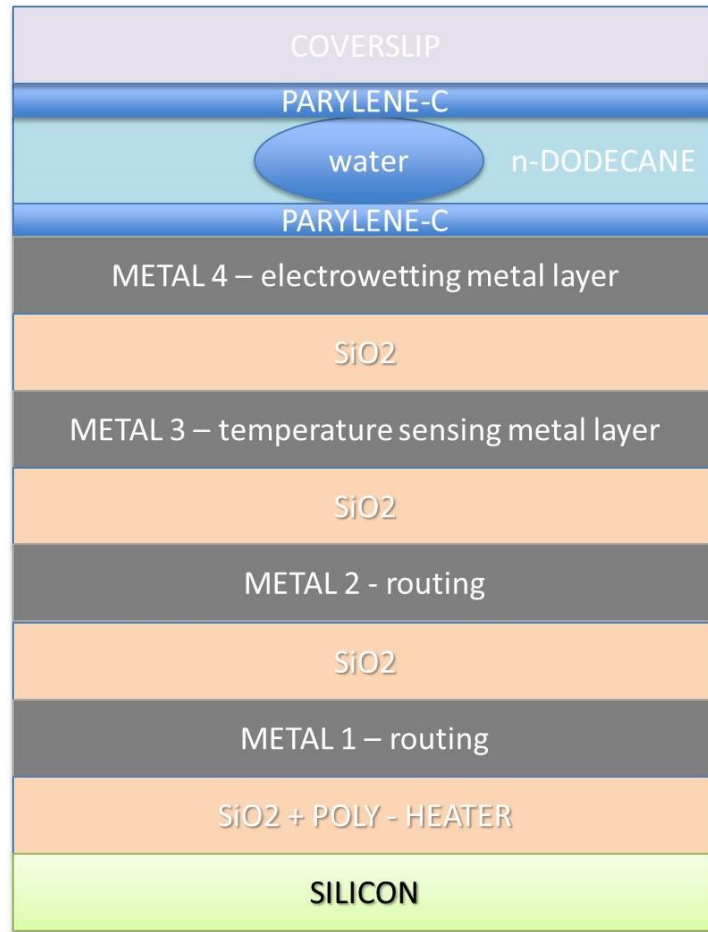Table 3-3: Device parameters used for COMSOL thermal modeling

Figure 3-10: Thermal stack simulated using COMSOL

FEM simulation (COMSOL) verified that the polysilicon resistors, given their sheet resistance and maximum allowable current levels, would be able to reach 94°C with a ramp time and surface infirmity suitable for performing PCR.   More specifically, the three polysilicon heaters, separated by 400µm and located as shown in Figure 3.11, provide even heating of the chip surface, allowing surface temperature variation of less than $\pm$ 1.5°C within 3 seconds of turning on. Each heater consists of a serpentine trace 5300-µm long and 20-µm wide with a nominal effective resistance of 270kΩ. In contrast, the temperature

sensors are approximately 80000-µm long and 0.67-µm wide with a room temperature resistance of 4.3kΩ and a temperature coefficient of 3.3×10^{-3}. The sensors are located 4µm below the reagent-containing droplet. Temperature calibration is performed using the techniques described in Section 4.1
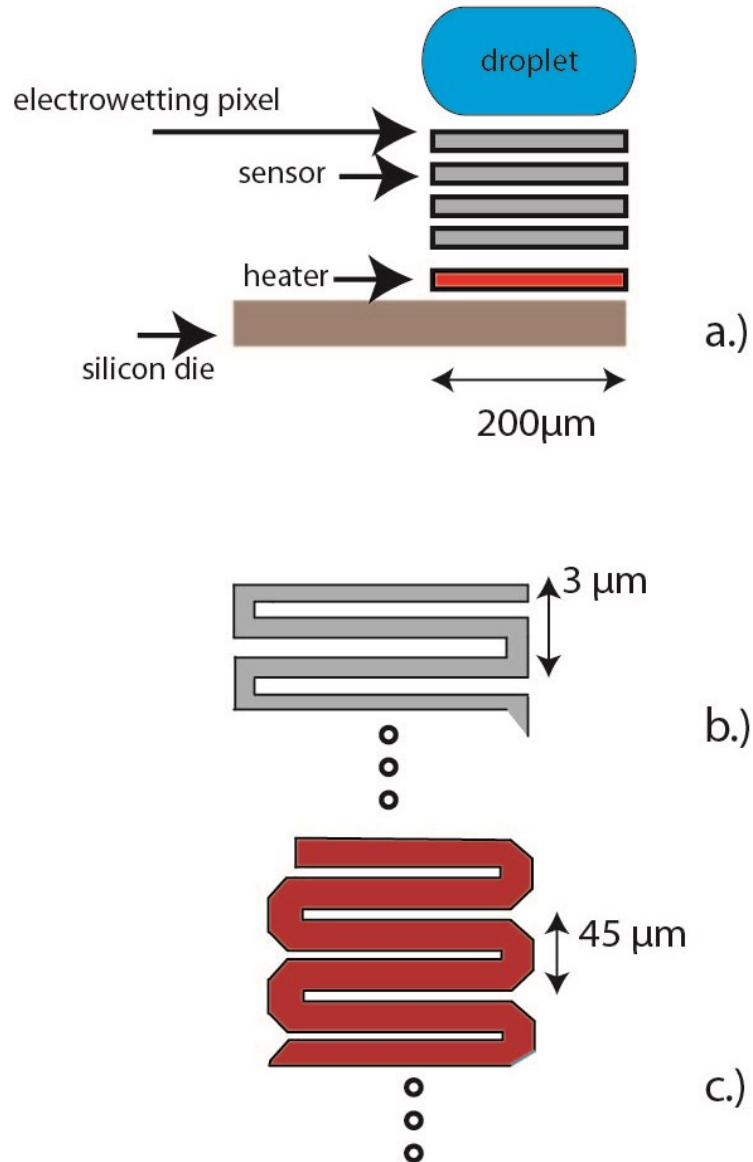

Figure 3-11: Sizing of on-chip resistive temperature sensor and heater

3.3 Integrated Single Photon Avalanche Diode [SPAD]

Avalanche photodiodes, which operate above the breakdown voltage in Geiger mode connected with avalanche-quenching circuits, can be used to count single photons and are thus referred to as Single photon Avalanche diodes (SPAD) [59] [60] [61] [62] [63]. In order to perform fluorescent measurements on the low intensity florescent signals emitted from the nanoliter droplets of QPCR reagent, SPAD's were selected owing to their small size [as small as 5um in diameter] and high sensitivity levels. Further highlighting the theme of this work is that the photodetectors, just as the heaters and EWOD droplet transport pixels, are perfectly matched to the form factor of the droplet itself.

3.3.1 SPAD implementation

For qPCR fluorescent measurements, a Single Photon Avalanche Diode (SPAD) is used. The device has been integrated into CMOS, located under one of the electrowetting pixels. Although an area of $100 \mu m^2$ has been removed from the aluminium pixel to enable photon transmission down to the SPAD, we observed no noticeable effects on the electrowetting-enabled droplet transport. The SPAD shallow P+ region has a diameter of 7.5 μm in an n-well of diameter 15 μm, shown in Figure 3.12.

The diode is biased beyond its reverse bias voltage by an overvoltage, V_{OV}. The device does draw any current until a photon striking the junction triggers an avalanche via

carrier multiplication. Fluorescence triggered avalanche events are counted over a set time period, the total count being proportional to the intensity of the fluorescent output of the intercalator dye and thus the progression of PCR.
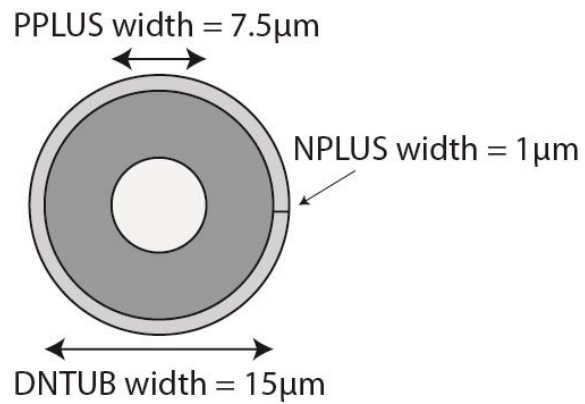

Figure 3-12: SPAD layout

3.3.2 Geiger mode operation

Geiger mode of operation of the SPAD requires a quenching circuit in order to reset the device. In our test setup, the SPAD is reset using a series resistor. When an avalanche is triggered, a current flows through the resistor and causes a significant voltage to be dropped across its terminals. As a result the voltage dropped across the diode is reduced and the current is halted as the diode is no longer in a high current region of operation. The associated RC time constant to return to a reverse bias of $(V_{RB} - V_{OV})$ defines the dead-time for the SPAD. In our device, a quenching resistance of 67 kΩ is used yielding maximum avalanche current levels of 10.3 μA and a dead-time of 0.5 μs with Vov of 3.5 V. With the passive quenching circuit configuration, the probability of after-pulsing is negligible. The device is not affected by noise events that are caused by charges that do not clear the multiplication region before the SPAD is reset. In order to use make use of the on-chip SPADs, the diodes must be disabled when the laser pulses but ready to trigger an avalanche when the dye is fluorescing. Our prototyping setup is shown in Figure 3.13.
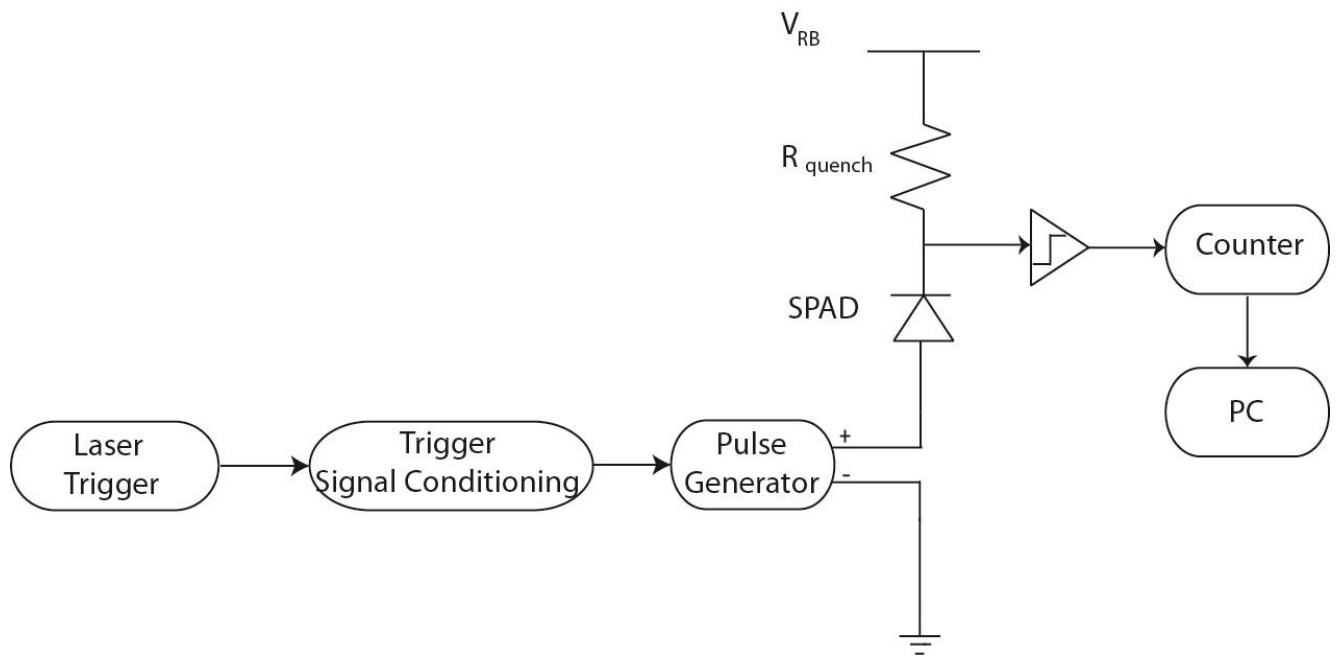
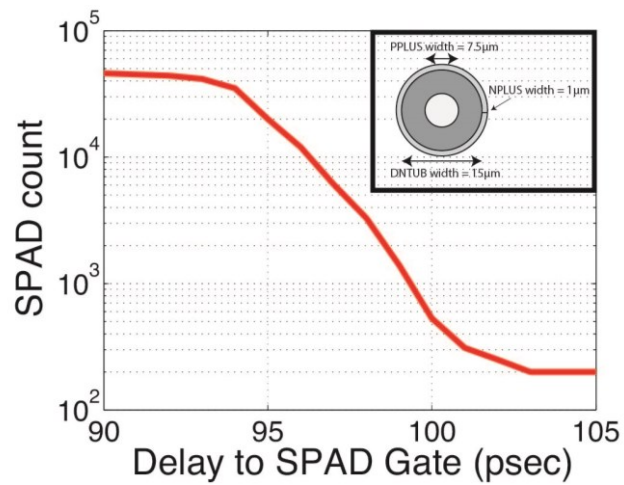Figure 3-13: SPAD implementation

Figure 3-14: SPAD calibration curve used to zero out effect of laser induced avalanche events

pulse stretching is performed using an analog filter with a 6dB high pass cutoff of 10kHz. This converts the 5mV signal to a 5V sinusoid. The amplified and filtered signal is fed into a pulse generator that outputs one pulse per period. The trigger delay and width of the pulse are used to tune the precise timing of the gating pulse. Picosecond adjustments are used to determine the optimal gating signal, fully eliminating triggering due to the applied laser pulse without losing excess sensitivity. The delay is swept to find the minimum delay at which the laser triggered avalanches are eliminated, shown in Figure 3.14. Note that our time gating scheme currently makes use of the bench-top Fianium tuneable laser. Future revisions of the device can make use of handheld time-gated laser devices.[64]

3.4 Device Packaging

The chip is mounted on a ball-grid-array package with SU-8 encapsulation of the wirebonds[65, 66, 67]. Since SU-8 is photo-patternable, the wirebonds are encapsulated and the active microfluidic area is patterned simultaneously, as shown in Figure 3.15. Similar work has been performed by Hammond and Cumming [68] using SU-8 for encapsulation integrated circuits onto custom designed FR-4 printed circuit boards. In their study, a cavity was drilled into the PCB into which the IC placed, requiring a 100μm thick layer of SU-8. Our work builds upon this approach and extends the concept to a wide variety of commercially available IC packages and professionally bonded chips. Given its robustness, our method can be generalized to any package geometry using SU-8 as thick as 1mm and without the need for custom drilled packages.
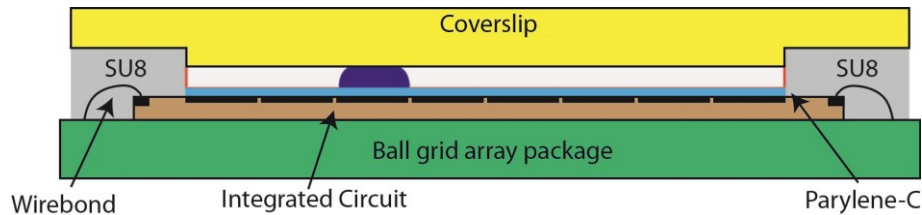

Figure 3-15: PCR chip packaging

The droplet array is covered with an indium-tin-oxide-(ITO)-coated polyethylene naphthalate (PEN) coverslip to support the correct electrostatics for droplet motion, shown in Figure 3.15. The height of each droplet is determined by the height of the addition made to the PEN coverslip. Special care is taken during the SU-8 process to ensure suitable planarity to allow tilt-free placement of the coverslip. Cast SU-8 is not fully baked prior to photolithographic exposure to allow a degree of pliability and is thus suitably flattened by the application of the exposure mask.

3.4.1 Thick SU-8 recipe and dielectric deposition

Our procedure for SU-8 encapsulation of wirebonded IC's is as follows: The BGA package is heated to 70°C in order to decrease SU-8 viscosity upon contact with the heated substrate. The SU-8 is poured directly from the bottle in order to minimize air bubbles. On a level hotplate [Electronic Micro Systems 1000-1], we slowly ramp the temperature from room temperature to 65°C and hold for 30 minutes. The temperature is then increased from 65°C to 95°C and held for 6.5 hours. The pre-bake concludes with a decrease ramp from 95°C to 25°C for the final 30 minutes. An SU-8 long-pass filter is used on the Karl Suss MA-6 mask aligner. Exposure is 6000mJ at 10mW. The sample is immediately placed on a room temperature hotplate and slowly ramped to 75°C over 5min. The sample temperature is held steady at 75°C for 25 minutes after which it is slowly cooled to room temperature over a span of 20 minutes. The device is soaked in 5mL of SU-8 Developer for 30 minutes. Stir agitation is provided using a magnetic stir bar at 60 rpm. The sample is first rinsed in isopropanol and then with water. Demonstration of aspect ratios of 10:1 have been demonstrated with this recipe for SU-8 thickness ranging from 500μm to 2mm. Figure 3.16 illustrates a 800μm thick SU-8 film with sidewalls of greater than 89°. Figure 3.17 illustrates a fully post-processed chip. Wirebonds have been encapsulated and the electrowetting active region exposed with use of SU-8.

Following the SU-8 patterning, a conformal coating of Parlyene-C is deposited atop the chip surface to provide adequate dielectric isolation. Total thickness of the Parylene-C layer is 2um. Deposition is performed using the Labcoter2 Parylene Deposition Chamber (Specialty Coating Services; Indianapolis, Indiana). To increase the hydrophobicity of the

dielectric layer, a 100nm thick layer of Teflon AF (DuPont, New York, New York) spin coated atop the Parylene-C. A volume of 10μL of Teflon® AF amorphous fluoroplastic resin in solution (6%WT) is added to the reservoir. The spin profile is as follows: Spin at 1500rpm for 45 seconds. The Teflon is baked at 125°C for 75 seconds.
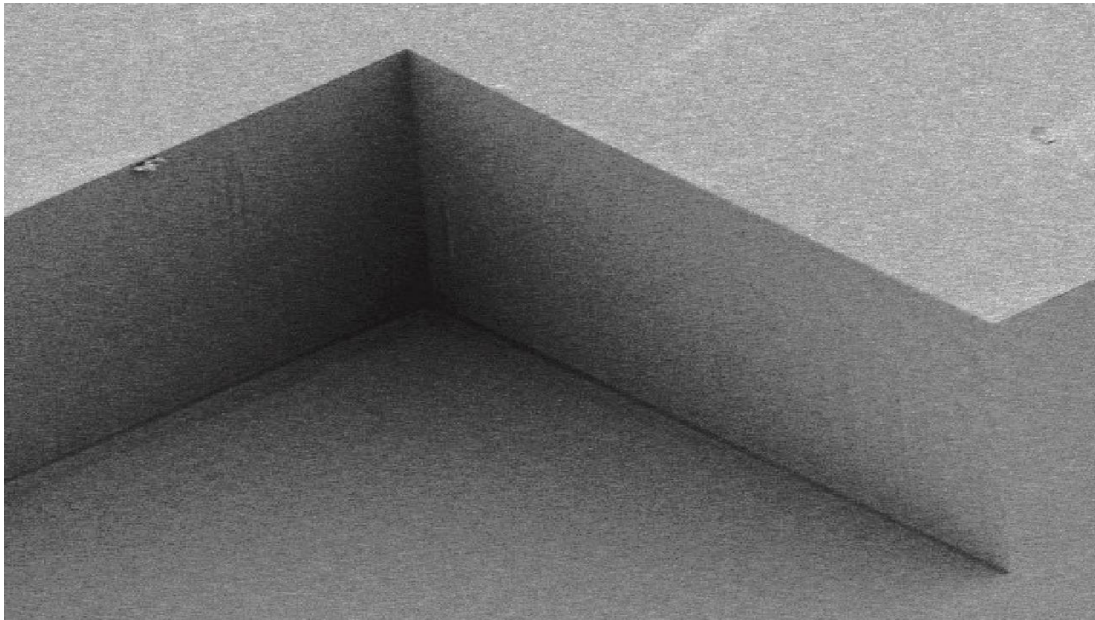
Figure 3-16: SEM micrograph of SU-8 800μm thick sidewalls using the developed high thickness recipe
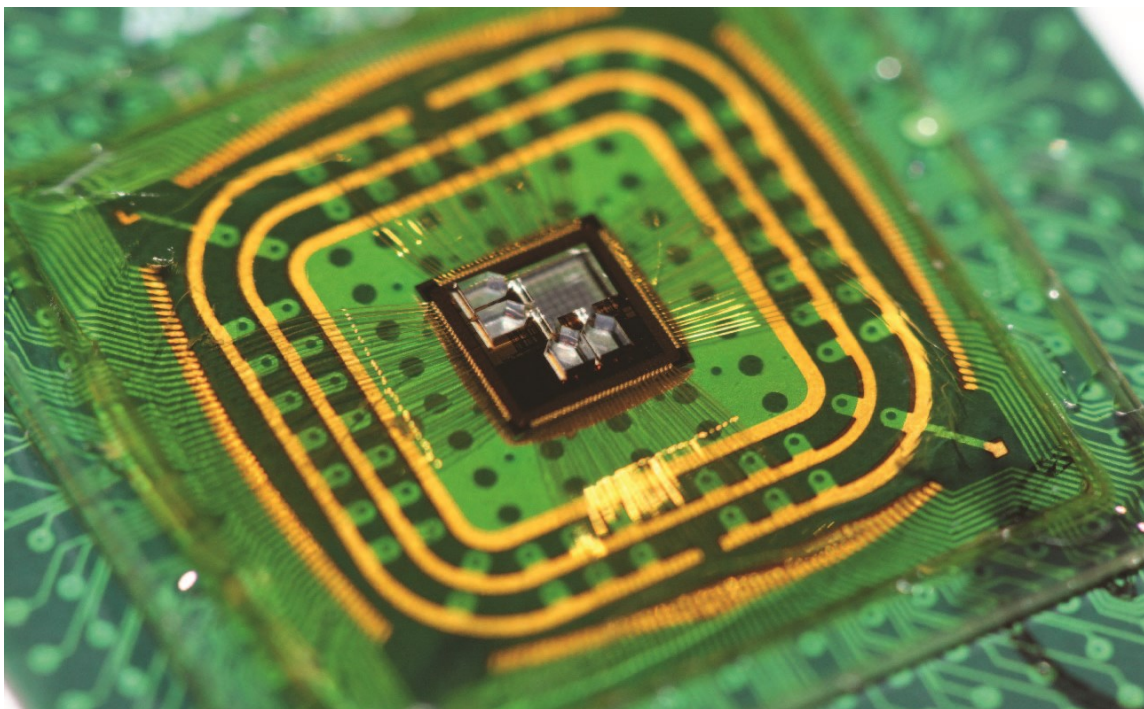

Figure 3-17: Photograph of an SU-8 encapsulated, wirebonded PCR chip on a BGA package

Chapter 4

Implementation of QPCR on CMOS

Following fabrication at the foundry and subsequent wirebonding to a custom BGA 272 package, each PCR chip underwent post-processing as described in Chapter 3 in order to encapsulate the wirebonds and define the active electrowetting droplet transport region. A custom PCB assembly was designed for device testing and included circuitry for controlling the heaters, taking readings from the temperature sensors, and performing Geiger mode measurements using the on-chip SPADs.

This chapter will first discuss the calibration of the on-chip temperature control feedback using a spatially resolved temperature mapping from custom designed DNA thermometer. We will then discuss the characterization of the on-chip SPADs and provide data confirming their adequate sensitivity for sensing the fluorescence from a nanoliter scale droplet in their passively quenched Geiger mode operation. The chapter culminates in a complete demonstration of all components of the chip working in unison. QPCR data is provided across a range of initial target DNA concentrations.

4.1 Integrated Temperature Sensor calibration using a 'DNA Thermometer'

As discussed in the previous section, temperature control is maintained on the surface of the chip with the use of integrated sensors and heaters. Current is passed through high-resistance polysilicon resistors to heat the chip. Resistive temperature sensors consisting of serpentine interconnect metal are calibrated to monitor the temperature. Temperature readings are accurate to $0.45^{o}C$. The temperature sensors are located 4um below the reagent-containing droplet. In order to correlate the serpentine resistive temperature sensor reading to the actual temperature of the droplet, we developed a method to produce a spatially resolved temperature mapping of the surface of the chip using DNA as the active temperature sensing material.

As discussed in the previous chapter, the method for surface temperature sensing builds upon previous work performed by Jeon et al [69] and Tashiro[70] using the large temperature sensitivity of the fluorescence lifetime of labeled DNA oligomers due to conformational changes in the DNA. The authors exploit the temperature-dependent fluorescent modulation of the spacing between a fluorescent dye and a designed sequence of DNA bases as a means of measuring changes in temperature. The higher the temperature, the faster is the conformational change and thus the shorter the fluorescence lifetime. The authors focus on obtaining an average temperature from an oligonucleotide sample is an Eppendorf tube, useful for calibrating a quantitative PCR machine for instance. We seek to extend previous work [69] and use DNA melting, as tracked by an intercalator dye, to obtain a two-dimensional temperature profile.

When excited with a broadband UV source, regions of high temperature will possess a higher concentration of single stranded DNA, manifest in reduced fluorescent emission intensity from the intercalator. Through careful calibration of the DNA temperature sensing solution, a fluorescence-to-temperature mapping is acquired. A single 12-base oligonucleotide can achieve a dynamic range of approximately 10°C. If several different oligonucleotides were combined in a single solution, the dynamic range of the thermometer can be extended seamlessly from 25°C to 95°C. This temperature sensitive DNA solution mixed with intercalator dye is placed directly on surface of the chip and sealed with the recessed coverslip, illustrated in Figure 4.1.
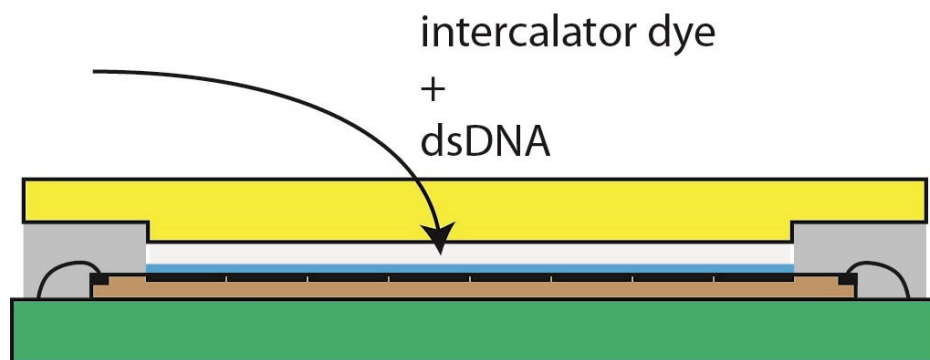

Figure 4-1: Double stranded DNA and intercalator dye placement for use in DNA thermometer-based calibrations

In order to optimize the dynamic range of the DNA thermometer, a DNA oligonucleotide with a broad melting profile is designed. DINAMELT is used to simulate oligonucleotide melting[71]. Special care was taken to avoid strands that exhibit self-folding tendencies. The goal is create a strand with highly linear melting profile over a specified temperature range, which we set to 10 degrees Celsius. Many factors influence the melting temperature and its slope   Long sequences (>50bp) with a random assortment of

nucleotides will typically have very high melting temperatures, approaching 94°C. Shorter sequences will have lower melting temperatures. The slope of the melting curve will be highly dependent on the sequence itself. Sequences with high concentration of guanine-cytosine pairs will have broad melting curves due to strength of the inter-base bonds. Care must be taken to avoid using too many G-C pairs to avoid difficulties in synthesis as well as to prevent excessive single strand folding. The DNA sequence AAAGGAAAGGAAAAGGAAAAGG, whose experimentally obtained melting curve is shown in Figure 4.2, is used to obtain the spatially resolved mapping optimized around 72°C.
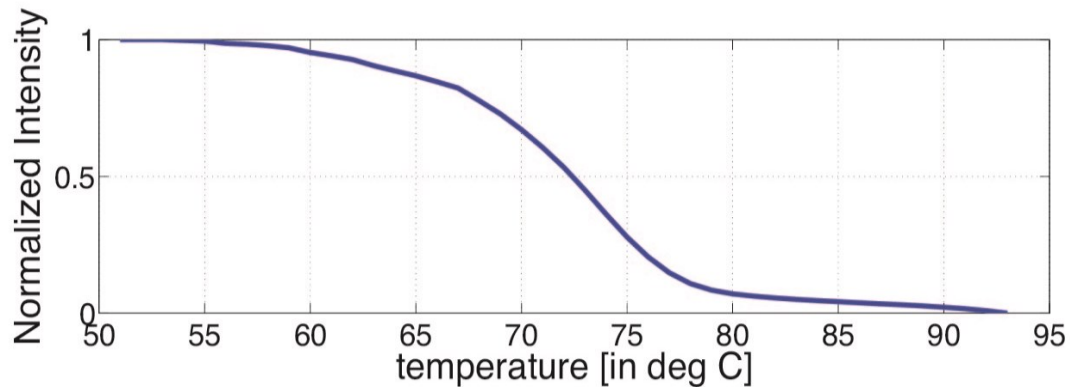

Figure 4-2: DNA melting curve for calibrating on-chip temperature control circuitry at 72°C

4.1.1 High resolution spatial temperature mapping using DNA melting

Figure 4.3 demonstrates the surface of the chip in thermal equilibrium measured with the DNA thermometer technique. In this example, the majority of the device surface ramps

from 25ºC to 72ºC in 9.4 seconds. Gradient are initially observed but once the device

reaches equilibrium at its set point, we observe suitable uniformity for qPCR at 10.8 seconds

after turning the heaters on. At this point, approximately 75% of the chip's surface is within

0.5ºC of the desired set point. The remaining 25% is within 1.5ºC.

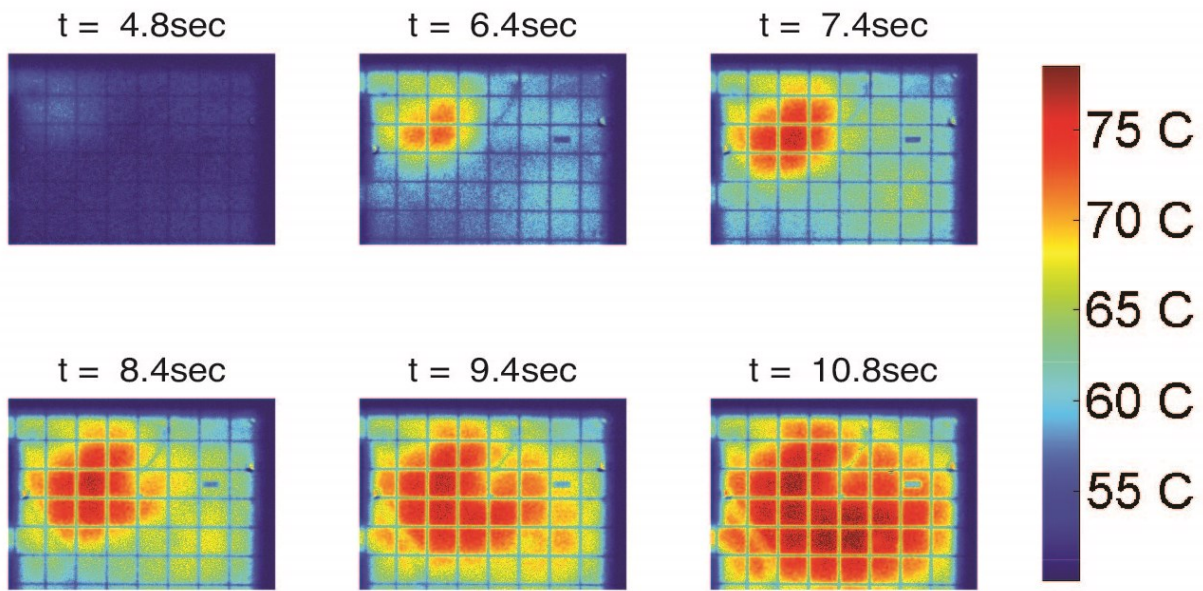## 4.1.2 Surface temperature uniformity


<u>Figure 4-3:</u> Demonstration of spatially resolved temperature mapping on the surface of the
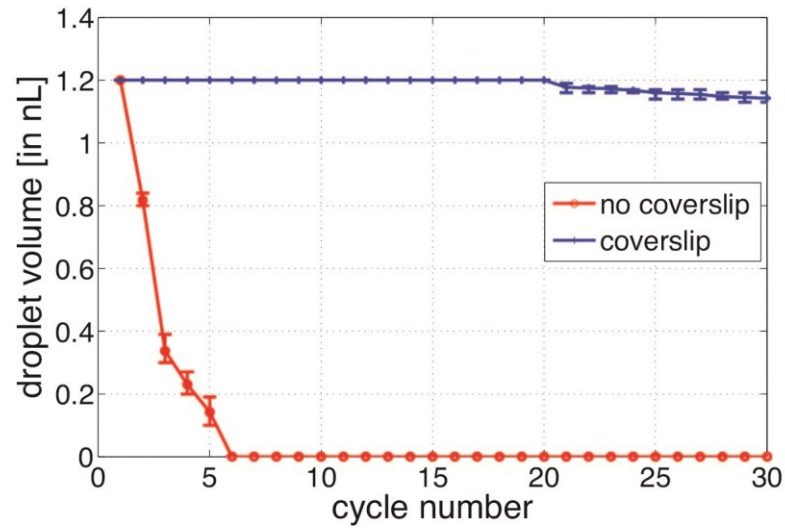PCR chip

4.2 Nanoliter volume droplet evaporation

Preliminary experimentation sought to perform electrowetting droplet transport and subsequent PCR thermal cycling on reagent-containing aqueous droplet exposed to air. However, as experimental droplet dimensions were reduced down to 1.2 nanoliters, evaporation led difficulties in carrying out a full PCR test run.

Droplet evaporation is reduced by immersion of the droplet in dodecane [72-75] and hermetic sealing of the reaction cavity on the chip. Figure 4.4a shows the rate of evaporation of 1.2 nanoliter droplets in air and in dodecane at 25ºC. . This evaporation rate of 20 picoliters per second makes this an impractical modality for qPCR. During active thermal cycling, however, even in dodecane, evaporation still occurs at an unacceptably high rate of 1.9pL per second (Figure. 4.4, b). By hermetically sealing the reaction cavity with the PEN coverslip, this evaporation rate is reduced to 6.3fL per second (Figure 4.4, b), resulting in a volume reduction of less than 1% during the 3600 sec that characterize a typical qPCR run.
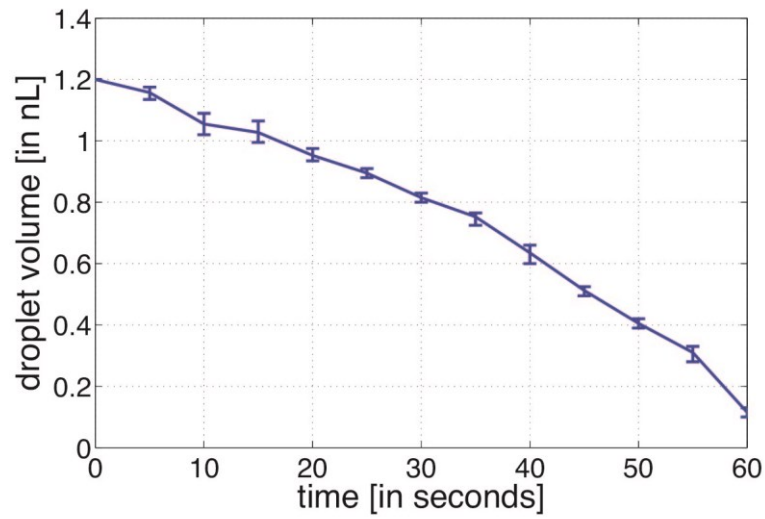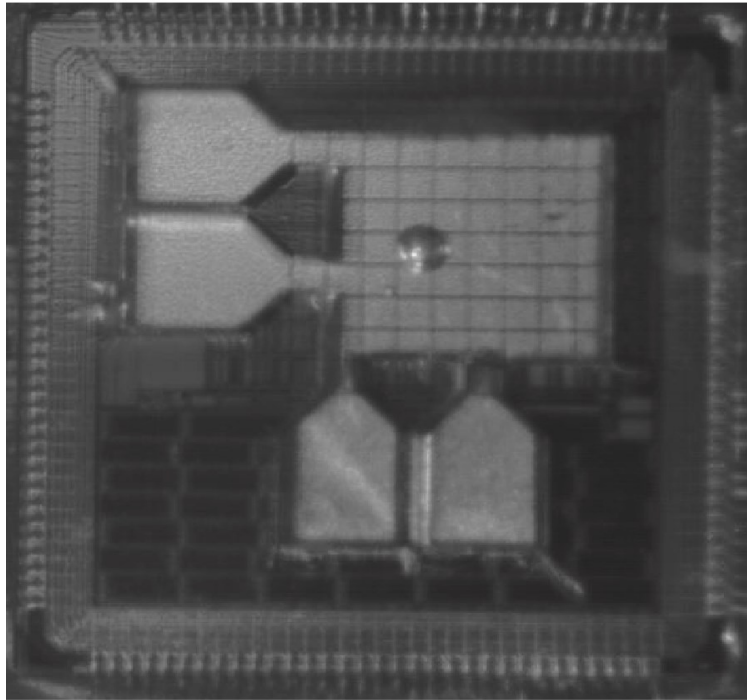
Figure 4-4: Evaporation of nanoliter droplets in air at 25°C and with/without dodecane immersing over PCR 30-stage thermal cycling profile

a.

b.

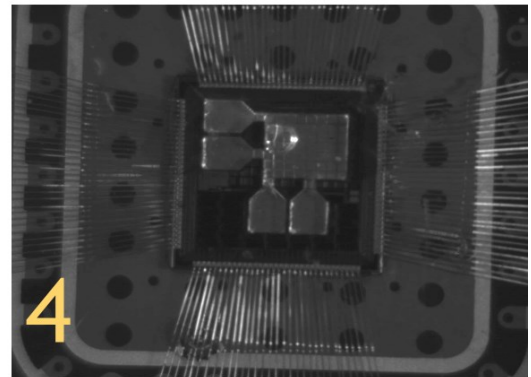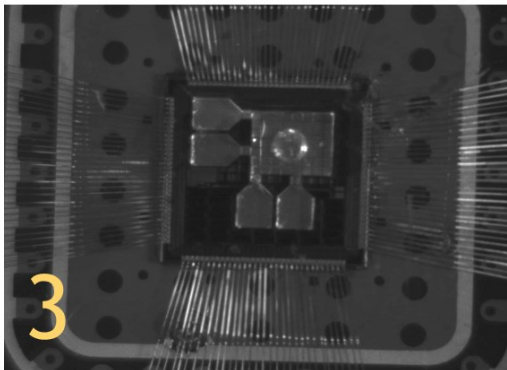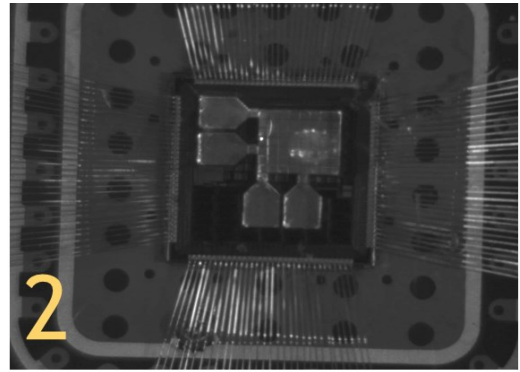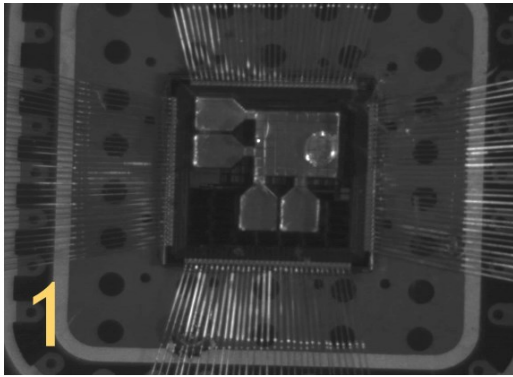Figure 4-5: Photograph of droplet on PCR chip electrowetting array

Figure 4-6: Droplet actuation using on-chip electrowetting circuitry

4.3 On-Chip SPAD performance

In order to integrate fluorescent detection, Geiger-mode SPADs with passive quenching are integrated on-chip. The SPADs employed here have a breakdown voltage of approximately 20V. Analysis is performed to find an optimal point between PDP and dark count rate. Operated at an overvoltage of 23.5V, they have a dark count rate of 100 Hz and a photon detection probability of better than 7.25% at 515 nm (Figures 4.7, 4.8, 4.9). On-chip fluorescence detection is often challenged by the need to reject the excitation source by over 50 dB in typical applications, which is not easily achieved because of the absence of adequate optical filters. In this case, we use a time-resolved measurement to achieve this background rejection. The laser excitation (at 500-nm) is pulsed and photons are detected from the fluorophores after the excitation source has been removed. Fluorescent data is collected following the elongation stage of each PCR cycle. SPAD detection limits are in the nanomolar regime (Figure 4.11).

4.3.1 Photon Detection Probability [PDP] and Dark Count Rate

Photon detection probability requires careful measurement across wavelength and across applied voltage. The readings were obtained as follows: A monochromator is used to generate precise incident wavelength. Integrating sphere ensures uniform photon distribution over a given diameter. An additional lens is placed against the aperture to collect the light. With a 25.4 mm focal-distance biconvex lens the power able to be collected by the photodetector is approximately 2 μW. This output intensity must be applied evenly (perfectly centered) atop both the SPAD under test as well as atop the photodetector used to

determine the intensity of the light at each given wavelength. The Thor Labs PM100D photodetector has an aperture diameter of 7.9mm, a maximum power of 200W and a minimum of 100 pW.

Prior to calculating the PDP, we must first obtain the photons per second (PPS) given as follows:

$$PPS = \frac{P}{hc/\lambda}$$
<div align="right">Equation 4.1</div>

where

P is the power read on the photodetector (minus the power read when the photodetector is dark),

h = Planck's constant = 6.626068 × 10-34 m2 kg / s,

c = 299 792 458 m / s

and the area of the photodetector is $A_{detector}$ in μm^2.

The photons per second per unit area given off by the light source is given as the PPS / $A_{detector}$. By multiplying this product by the area of the SPAD, $A_{SPAD,}$ the result is the photon flux seen by the SPAD. The total number of photons per integration window, T, then, is the SPAD photon flux multiplied by the integration window length. The number of electrons you can measure divided by the number of photons there are gives the QE. The number of hits/photon seen gives the PDP. PDP, is thus given as

$$PDP = \frac{SPAD\ HITS}{\frac{PPS \cdot T}{A}}$$
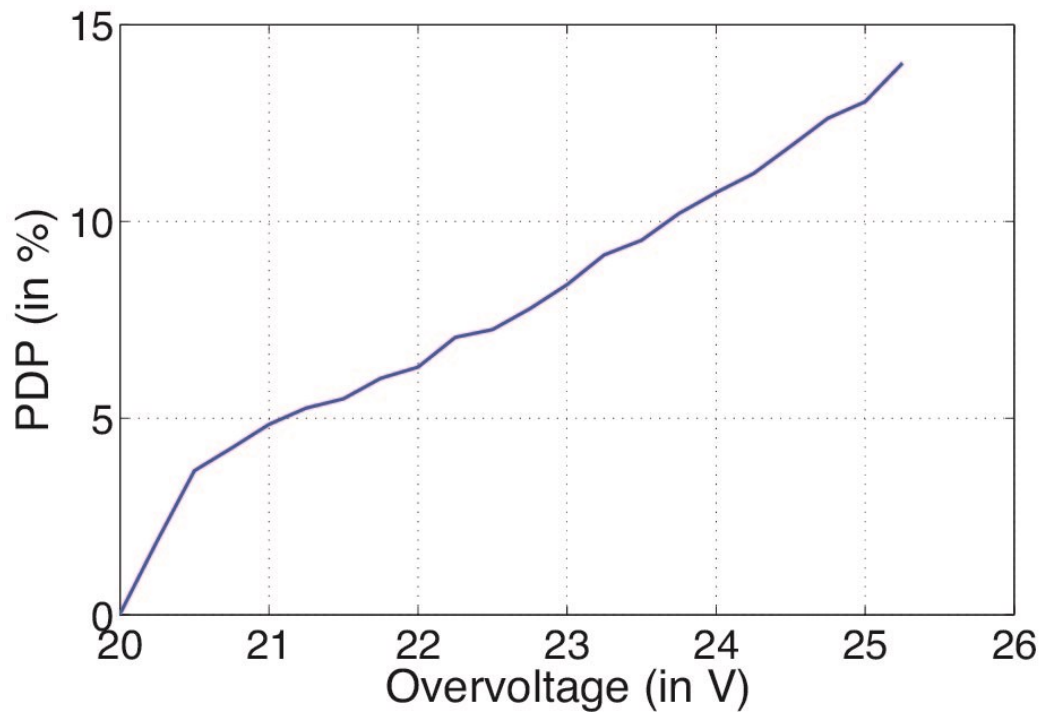<div align="right">Equation 4.2</div>

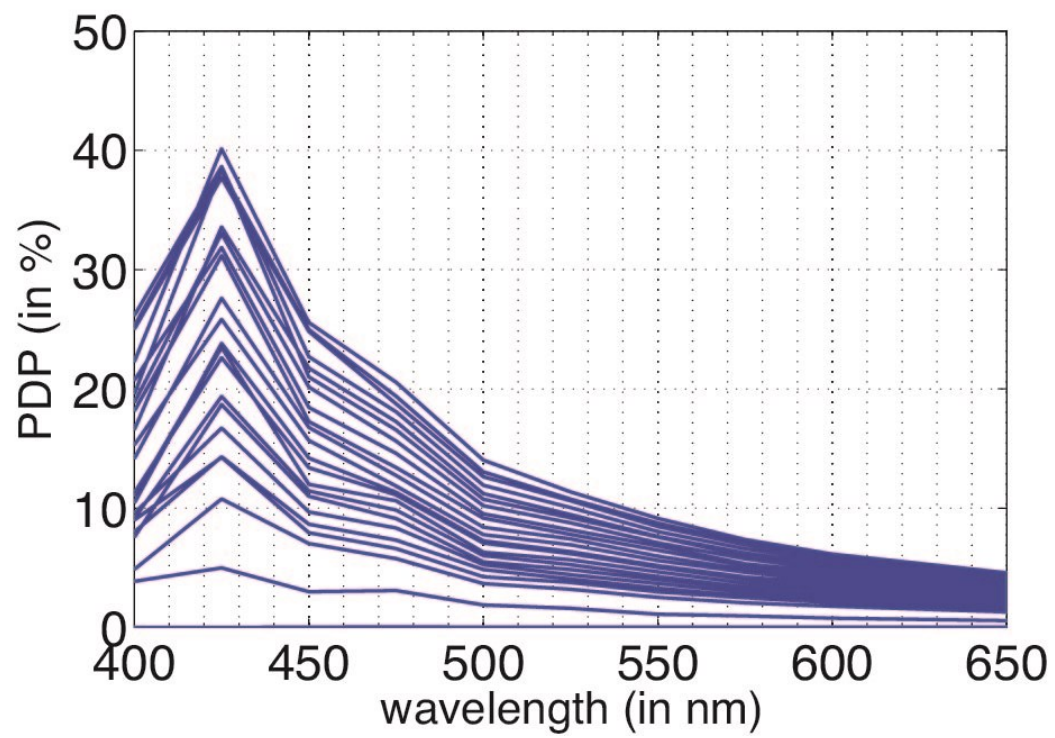Figure 4-7: SPAD PDP versus applied voltage at 25C for wavelength of 500nm

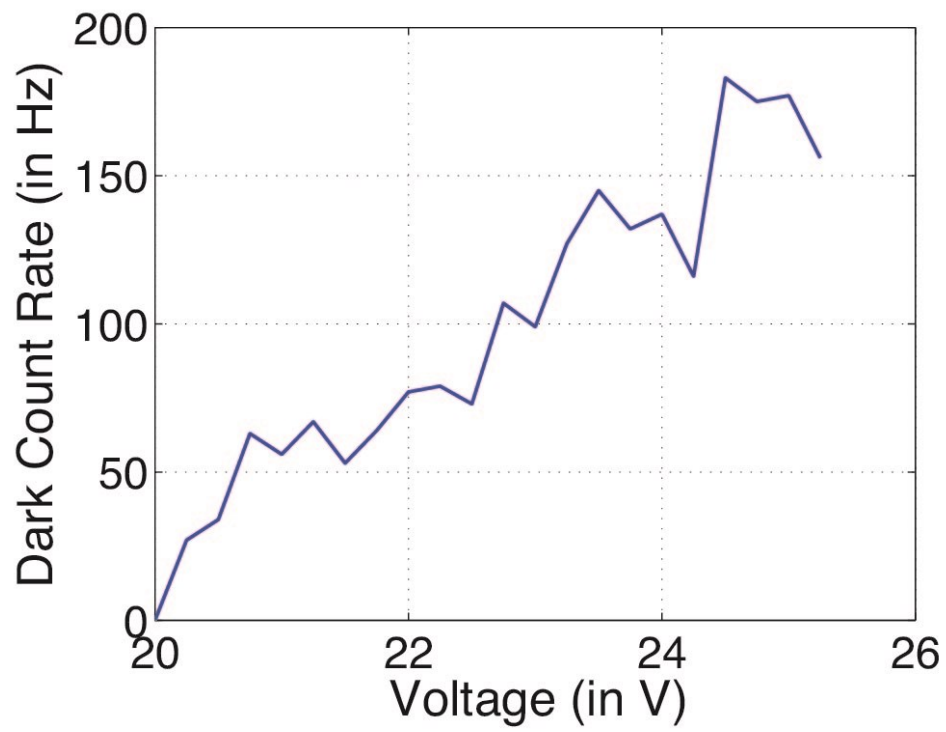Figure 4-8: SPAD PDP versus wavelength at 25ºC

Figure 4-9: SPAD Dark count rate versus applied voltage at 25ºC
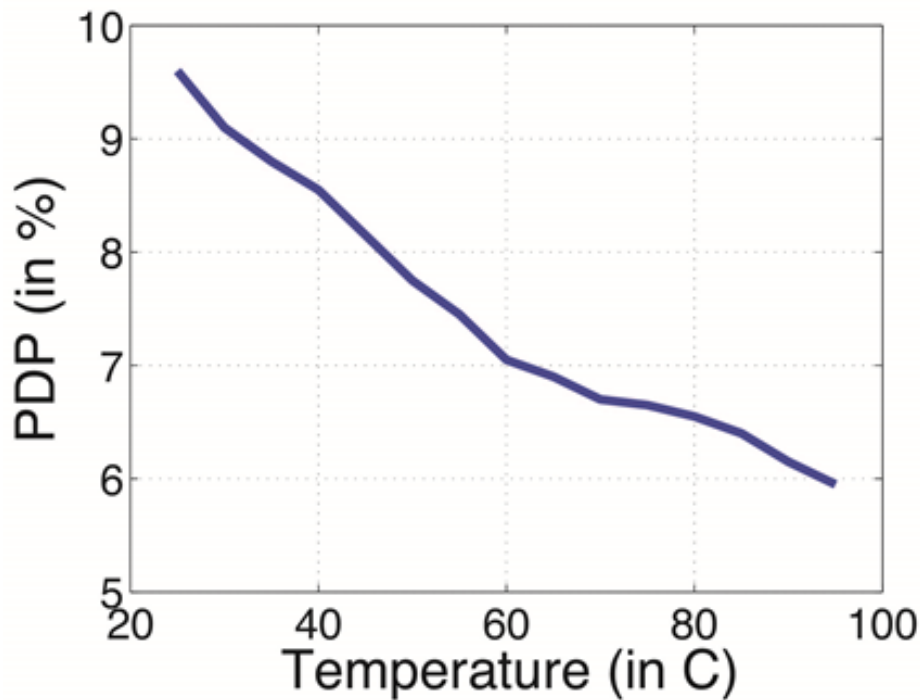
Figure 4-10: SPAD PDP at 23.5V over temperature

SPAD sensitivity to temperature was explored during the testing of the chip. We observed a decrease in the PDP of the SPADs with increasing temperature (Figure 4.10). Although we expected a higher PDP due to increased dark count noise, we observed the converse. We attribute this decrease in sensitivity to the temperature dependence the impact ionization coefficients.

Given this finding, we have two options when performing qPCR. When measuring the fluorescence at the conclusion of the elongation stage, we can turn off all of the on-chip heaters in order to preserve the full room temperature sensitivity of the photodiodes. Alternatively, as presented in the paper, the heaters can be left on and the decrease in sensitivity traded for time savings.

4.3.2 Limit of detection

Figure 4.11 shows a full calibration curve of SPAD counts with an integration time of 1 second as a function of dsDNA concentration with EvaGreen 20X intercalator dye (Biotium, Hayward, USA) for a few representative temperatures. Fluorescent data is collected following the elongation stage of each PCR cycle. SPAD detection limits are in the nanomolar regime, limited by SPAD dark count. The readings taken at 50°C leave the noise floor at a double- stranded DNA concentration of approximately 1.7 μM. The curve exhibits approximately linear behavior at higher concentrations of DNA and thus higher incident fluorescent emission intensity. The exponential increase just as the curve leaves the noise floor can be attributed to a combination of the integration time and the non-linear scattering of low-intensity light at the Teflon/Parylene interface. Note that as the temperature increases, the curve shifts to the right, indicating a decrease in overall sensitivity.
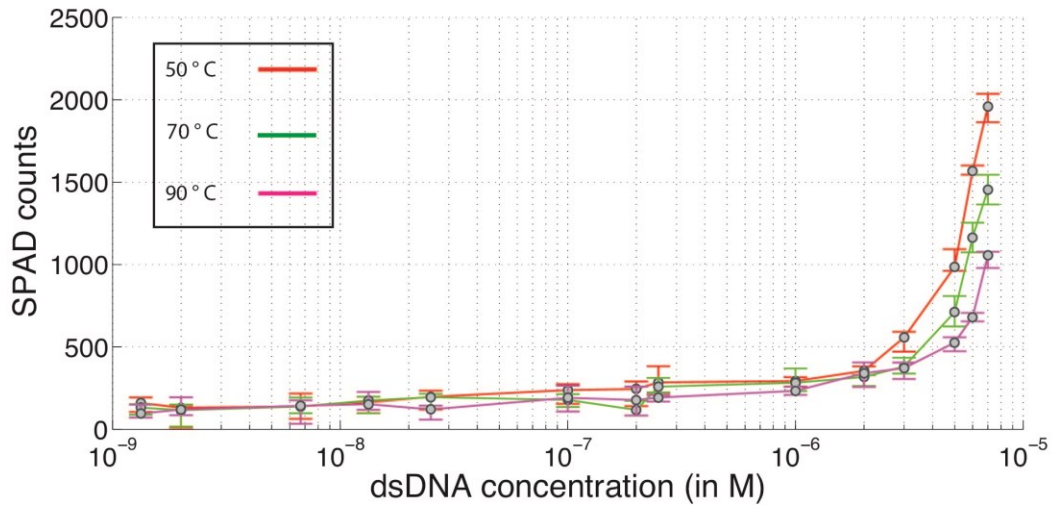
Figure 4-11: SPAD limit of detection for dsDNA (13bp) tagged with an intercalator dye at room temperature

4.4 Real-time Quantitative PCR analysis

A custom printed circuit board was assembled for the testing of the PCR chip, shown below in Figure 4.12. The core component of this system is a field programmable gate array development kit that is configured for USB-based communication to MATLAB. Using this setup allows for seamless temperature measurements, fluorescence measurements, and electrowetting droplet transport control.
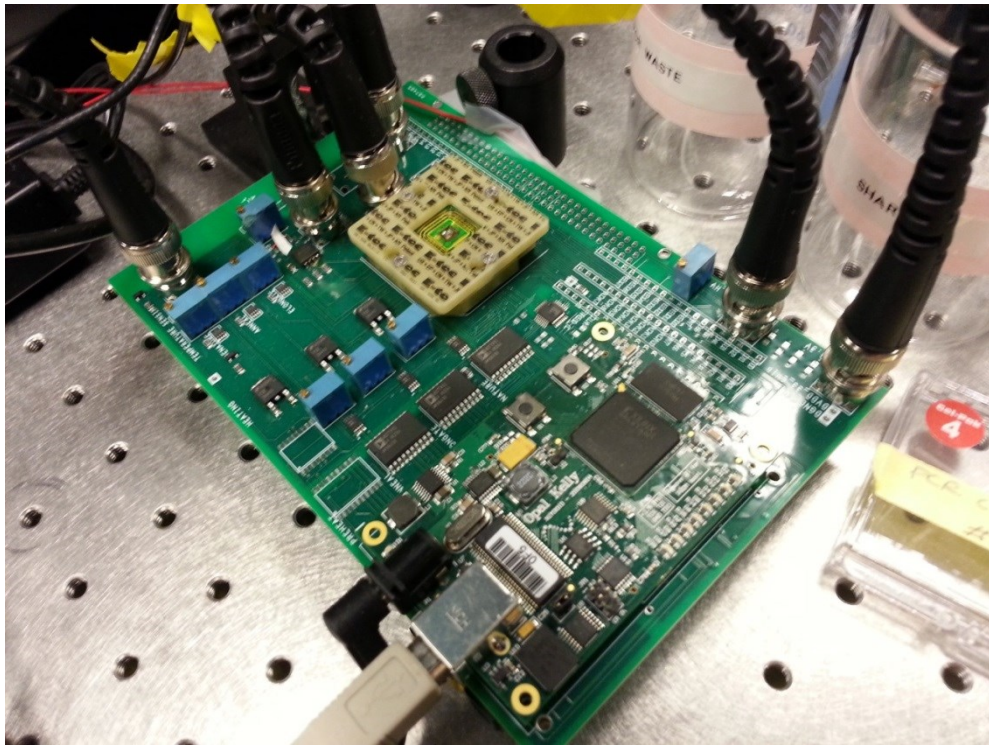
Figure 4-12: Printed Circuit Board for PCR Chip

4.4.1 On-chip heating profile

Readings from the center resistive temperature sensor are shown in Figure 4.13. The chip

heats at a maximum rate of 4°C per second. With the use of our P-D control loop, the surface heats from 72°C to 94°C in 11sec, from 94°C to 60°C in 13seconds, and from 60°C to 72°C in 8 seconds. The maximum ripple observed was 0.45°C.

Note that no active cooling devices such as fans or Peltier electrodes were used when ramping from the denaturing to the annealing steps. Cooling at maximum rate of -3°C per second is enabled due to heat sinking through the silicon substrate.

a.)

b.)

Figure 4-13: On-chip temperature profile as measured with integrated resistive temperature sensors

4.4.2 Analysis of qPCR on CMOS

As a proof-of-concept for our device, we amplify and detect a 364-base sequence coding as a characteristic sequence for *S. aureus*.
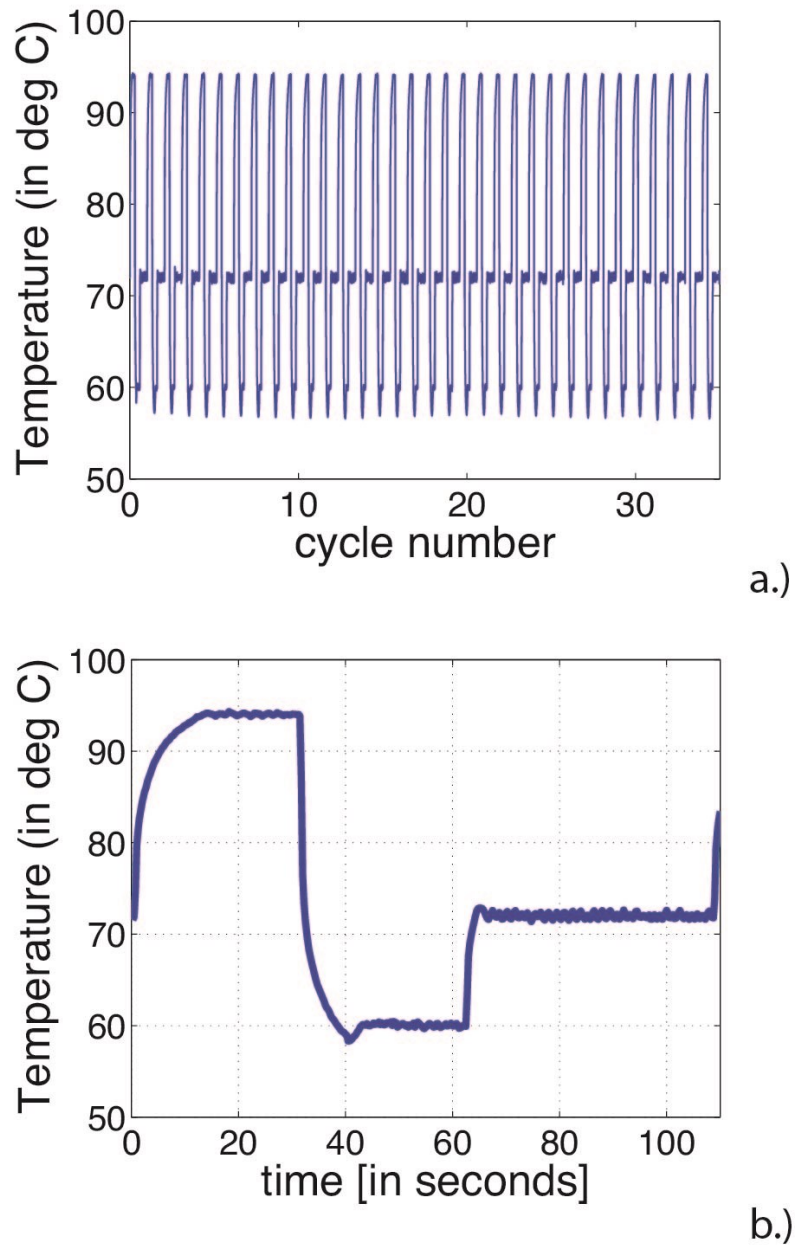
Figure 4.14 shows qPCR data from individual droplets with serial dilutions of the target strand from 1000 down to 1 copy per droplet. Each 1.2 nanoliter test droplet comes from mixing PCR mix (Norgen Biotek Corporation, Thorold, Canada), intercalator dye, DNA target, and buffer. The reagent consumption per qPCR test is reduced more than 40000-fold compared to conventional RT-PCR assays.

We observed repeatable amplification at all starting concentrations (Figure 4.14). For concentrations over the full range of the data, we obtained the expected linear relationship between cycle threshold and the logarithm of initial concentration (Figure 4.15).
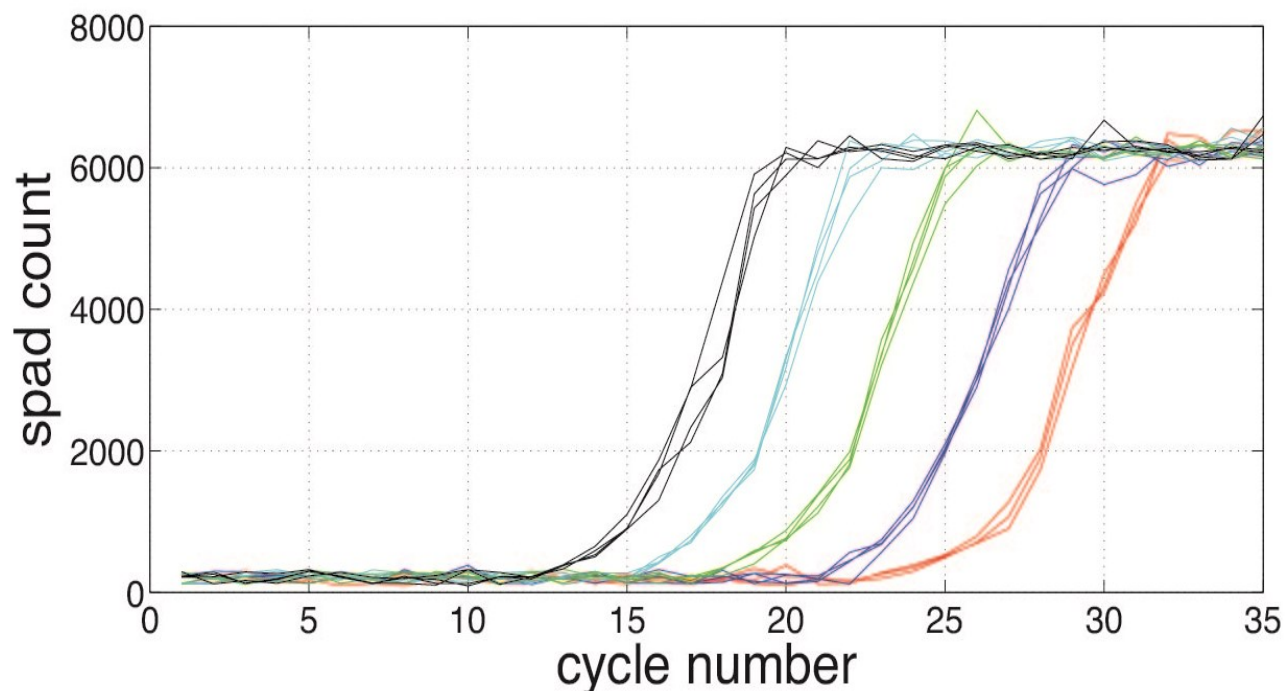

Figure 4-14: Real-time quantitative PCR data is plotted with respect to cycle number. Initial concentration of the DNA target is swept from 10000 copies/droplet down to 1 copy/droplet.
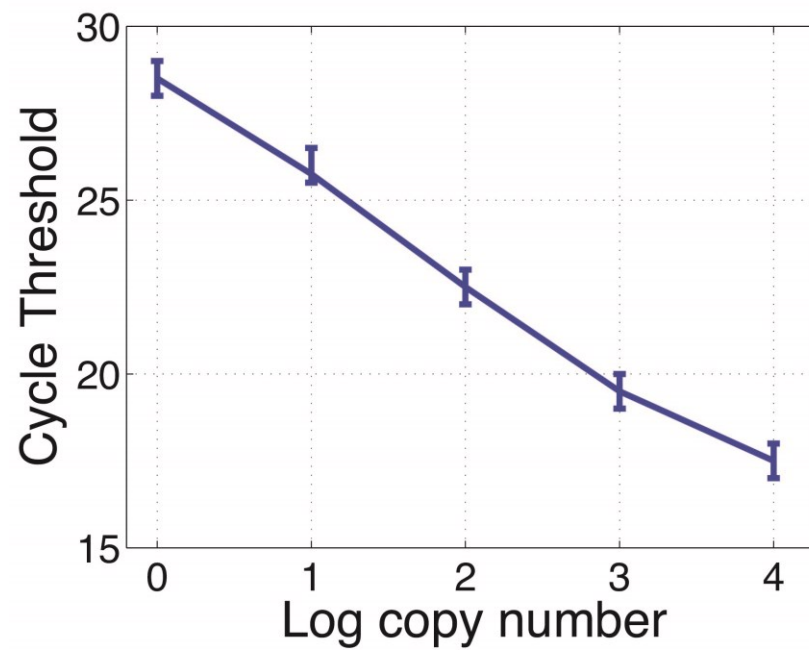
Figure 4-15: Cycle threshold as a function of initial target concentration given in terms of copy number

The non-specific binding of biomolecules to the surface of ParyleneC/Teflon AF dielectric has been shown to degrade the surface's hydrophobicity. [76] This factor was evaluated on our test chip using droplets containing the S. aureus PCR cocktail. The threshold voltage necessary for droplet actuation was plotted as a function of number of actuations (Figure 4.16). This test consisted of a 1.3nL droplet being transported between two adjacent electrowetting pixels. Note that a significant increase in the necessary electrowetting actuation voltage occurs after approximately 200 actuations, allowing for satisfactory lifetime of a disposable medical device.
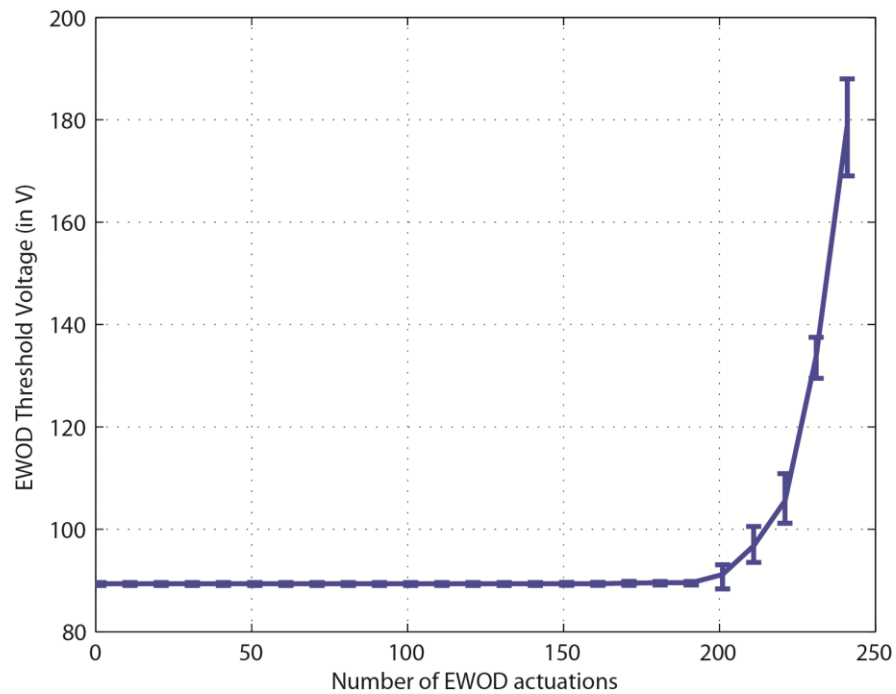
Figure 4-16: Long-term EWOD droplet transport testing

The hydrophobic interaction between water, dodecane, and electrowetting surface is expected to show dependence on temperature [77]. The threshold voltage necessary for droplet actuation was plotted as a function of temperature (Figure 4.17). This test consisted of a 1.3nL droplet being transported between two adjacent electrowetting pixels. Note that a significant increase in the electrowetting threshold voltage for our particular configuration occurs after 110°C. This operating range ensures electrowetting given our 90V actuation voltage across a temperature range suitable for performing PCR.
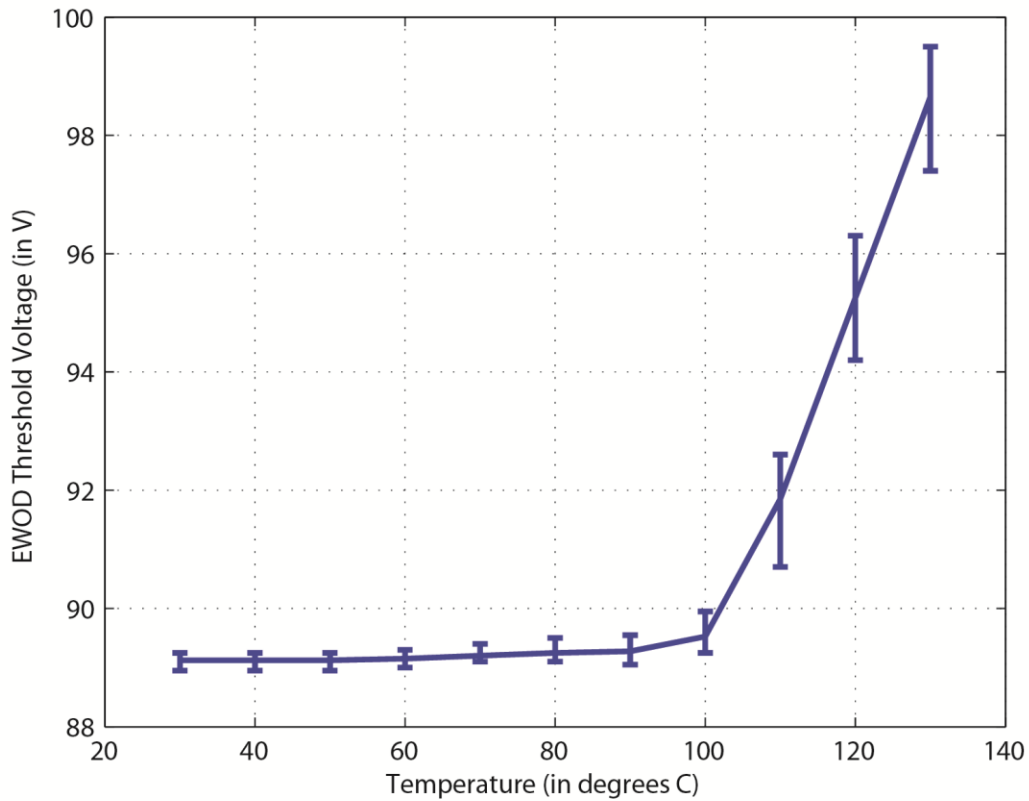
Figure 4-17: Effects of temperature on EWOD droplet transport threshold voltage

Chapter 5:

Conclusion

5.1 Summary of this work

This thesis demonstrated reliable and accurate qPCR diagnostics on the surface of a CMOS IC. All of the sensing and actuation have been embedded within a 4mm x 4mm lab-on-chip device. Temperature control, droplet-based microfluidic transport, and SPAD-based fluorescence measurements were combined to perform qPCR on the *S. aureus* test sequence. Initial target copy numbers as low as 1 copy per 1.2 nanoliter droplet could be reliably amplified and detected.

By leveraging the existing fabrication infrastructure of silicon IC foundries, lab-on-chip devices can seamlessly combine high sensitivity sensing and actuation with sophisticated post-processing all on a single chip.

5.1.1 Original Contributions

This work has made several original contributions to the fields of microelectronics, biosensors, and genetic diagnosis, including the following:

- Complete integration of heating control, electrowetting-enabled droplet transport, and Single Photon Avalanche Diode Geiger mode fluorescent detection on a CMOS die

- Demonstration of the DNA melting curve thermometer for taking spatially resolved temperature mapping of an IC surface

- Simultaneous IC microfeature patterning and wirebond encapsulation using ultra-thick SU-8 photopatternable epoxy

- QPCR performed reliably on the surface of a CMOS integrated circuit

5.2 Future directions

The device described in this work should serve as a template for future devices and proof that hardware/instrumentation can be adequately scaled to match the form factor of the test specimen droplets under investigation. Beyond the proof-of-concept presented in this work, the following steps can be taken to bring to further develop this lab-on-chip device.

- **Increase parallelization**

  In this work, one set of PCR primers was used for a given QPCR run. Future revisions of the chip should include more channels for implementation of multiple primer sets. The more primers that are able to act upon the DNA target, the more information we can gather for each screening.

- **Cross Contamination Study**

  Rigorous analysis of potential cross contamination of different target DNA samples should be performed and adequate cleaning protocols determined.

- **Miniaturization of Laser excitation hardware**

  Florescent dye was excited with the use of a bench top tunable laser. Future iterations of the device will utilize a laser diode integrated onto a portable PCB to create a truly point of care prototype.

- **Use of live cells**

  Demonstration of QPCR was performed using custom synthesized DNA target oligonucleotide. While appropriate for device verification and proof-of-concept testing, in order to create a truly point-of-care tool, the device must be capable of

operating on a live biological sample. Additional modules must be built in to the system to enable lysing of the cells and subsequent DNA purification prior to entering the QPCR detection protocol.

5.3   Final Thoughts

No electrical engineering thesis is complete without a reference to Moore's Law of transistor scaling. I hope that this work contributes to greater use of CMOS in unconventional applications in the post-Moore era. However, I also hope that this work contributes to a trend that has been in place for millennia before Moore and his observation regarding transistor scaling. I refer to the trend of Disease Diagnostics scaling. Let us rewind to 300 BC. At this point, Hippocrates advocates the examination of urine in order to diagnose disease. Continuing along recorded history, in 1770 John Hill introduces a method of obtaining specimens for microscopic study, and in 1830 Gerardus Mulder performs the first elemental chemical analysis of proteins. From a jar of urine to a single cell down to the protein level, the object on which we have performed diagnosis has been getting smaller and smaller yet the relevant information it provides increases.

Fast forward to today, and we are witness to the application of immunosorbent assays and DNA sequencing. The biological sample being operated on is getting smaller and smaller, and that particular sample, despite reduction in size by a factor of 1000 reveals 1000 times more information than its bulk counterpart. I hope that my work in scaling the instrumentation with which diagnosis is performed is able to contribute to ever smaller biomedical devices capable of ever more meaningful diagnoses.

References

1   Southern, E. M. "Detection of specific sequences among DNA fragments separated by gel electrophoresis. *Journal of Molecular Biology* **98**, 503-517 (1975).

2   Mullis, K. Process for amplifying nucleic acid sequences. *US Patent 4,683,202.*

3   Saiki, R. G., D.; Stoffel, S.; Scharf, S.; Higuchi, R.; Horn, G.; Mullis, K.; Erlich, H. Primer-directed enzymatic amplification of DNA with a thermostable DNA polymerase. *Science* **239**, 487–491 (1988).

4   Borte, S. *et al.* Neonatal screening for severe primary immunodeficiency diseases using high-throughput triplex real-time PCR. *Blood* **119**, 2552-2555, doi:10.1182/blood-2011-08-371021 (2012).

5   Yang, S. *et al.* Lack of protein 4.1G causes altered expression and localization of the cell adhesion molecule nectin-like 4 in testis and can cause male infertility. *Molecular and cellular biology* **31**, 2276-2286, doi:10.1128/MCB.01105-10 (2011).

6   P. Vannuffel, J. G., H. Ezzedine, B. Vandercam, M. Delmee, G. Wauters, and J. L. Gala. Specific detection of methicilin-resistant Staphylococcus species by multiplex PCR. *J. Clin. Microbol* **33**, 2864 (1995).

7   Fang, H. & Hedin, G. Rapid Screening and Identification of Methicillin-Resistant Staphylococcus aureus from Clinical Samples by Selective-Broth and Real-Time PCR Assay. *Journal of Clinical Microbiology* **41**, 2894-2899, doi:10.1128/jcm.41.7.2894-2899.2003 (2003).

8   Honore-Bouakline, S., Vincensini, J. P., Giacuzzo, V., Lagrange, P. H. & Herrmann, J. L. Rapid Diagnosis of Extrapulmonary Tuberculosis by PCR: Impact of Sample Preparation and DNA Extraction. *Journal of Clinical Microbiology* **41**, 2323-2329, doi:10.1128/jcm.41.6.2323-2329.2003 (2003).

9   G T Noordhoek, A. H. K., G Bjune, D Catty, J W Dale, P E Fine, P Godfrey-Faussett, S N Cho, T Shinnick and S B Svenson. Sensitivity and specificity of PCR for detection of Mycobacterium tuberculosis: a blind comparison study among seven laboratories. *J. Clin. Microbol* **32**, 277 (1994).

10   Hagan, K. A. *et al.* An integrated, valveless system for microfluidic purification and reverse transcription-PCR amplification of RNA for detection of infectious agents. *Lab on a chip* **11**, 957-961, doi:10.1039/c0lc00136h (2011).

11   Srinivasan, V., Pamula, V. K. & Fair, R. B. Droplet-based microfluidic lab-on-a-chip for glucose detection. *Analytica Chimica Acta* **507**, 145-150, doi:10.1016/j.aca.2003.12.030 (2004).

12   Srinivasan, V., Pamula, V. K. & Fair, R. B. An integrated digital microfluidic lab-on-a-chip for clinical diagnostics on human physiological fluids. *Lab on a chip* **4**, 310-315, doi:10.1039/b403341h (2004).

13   Hatch, A. C. *et al.* 1-Million droplet array with wide-field fluorescence imaging for digital PCR. *Lab on a chip* **11**, 3838-3845, doi:10.1039/c1lc20561g (2011).

14   Hunt, T. P., Issadore, D. & Westervelt, R. M. Integrated circuit/microfluidic chip to programmably trap and move cells and droplets with dielectrophoresis. *Lab on a chip* **8**, 81-87, doi:10.1039/b710928h (2008).

15   Rouet, F. *et al.* Transfer and evaluation of an automated, low-cost real-time reverse transcription-PCR test for diagnosis and monitoring of human immunodeficiency virus type 1 infection in a West African resource-limited setting. *J Clin Microbiol* **43**, 2709-2717, doi:10.1128/JCM.43.6.2709-2717.2005 (2005).

16   Auerswald, C. L., Sugano, E., Ellen, J. M. & Klausner, J. D. Street-based STD testing and treatment of homeless youth are feasible, acceptable and effective. *The Journal of*

adolescent health : official publication of the Society for Adolescent Medicine **38**, 208-212, doi:10.1016/j.jadohealth.2005.09.006 (2006).

17   M. Mimiaga, S. R., S. Bland, M. Skeer, K. Cranston, D. Isenberg, B. Vega, K. Mayer. Health System and Personal Barries resulting in decreased utilization of HIV and STD Testing Services among At-risk Black men who have sex with men in Massachusetts. *AIDS Patient Care and STDs* **23**, 825-835 (2009).

18   Mickey Urdea, L. A. P., Stuart S. Olmsted, Maria Y. Giovanni, Peter Kaspar, Andrew Shepherd, Penny Wilson, Carol A. Dahl, Steven Buchsbaum, Gerry Moeller & Deborah C. Hay Burgess. Requirements for high impact diagnostics in the developing world. *Nature*, 73-79 (2006/11/22/online).

19   D. V. Cousins, S. D. W., B. R. Francis, B. L Gow. Use of polymerase chain reaction for rapid diagnosis of tuberculosis. *J. Clin. Microbiol* **30**, 255-258 (1992).

20   L.Tapp, L. M., E. Rennel, M. Wik, A.C. Syvanen. Homogeneous Scoring of Single-Nucleotide Polymorphisms: Comparison of the 5'-Nuclease TaqMan Assay and Molecular Beacon Probes. *BioTechniques* **28**, 732-738 (2000).

21   K. Livak, S. F., J. Marmaro, W. Giusti, K. Deetz. Oligonucleotides with fluorescent dyes at opposite ends provide a quenched probe system useful for detecting PCR product and nucleic acid hybridization. *Genome Res.* **4**, 357-362 (1995).

22   R. Noble, J. F. Use of SYBR Green I for rapid epifluorescence counts of marine viruses and bacteria. *Aquatic Microbial Ecology* **14**, 113-118 (1998).

23   Li, Y.-D. *et al.* A cost-effective high-resolution melting approach using the EvaGreen dye for DNA polymorphism detection and genotyping in plants. *Journal of integrative plant biology* **52**, 1036-1042, doi:10.1111/j.1744-7909.2010.01001.x (2010).

24   Abdelgawad, M. & Wheeler, A. R. The Digital Revolution: A New Paradigm for Microfluidics. *Advanced Materials* **21**, 920-925, doi:10.1002/adma.200802244 (2009).

25   Cho, S. K., Moon, H. & Kim, C.-j. Creating, transporting, cutting, and merging liquid droplets by electrowetting-based actuation for digital microfluidic circuits. *Journal of Microelectromechanical Systems* **12**, 70-80, doi:10.1109/JMEMS.2002.807467 (2003).

26   Lee, J. Electrowetting and electrowetting-on-dielectric for microscale liquid handling. *Sensors and Actuators A: Physical* **95**, 259-268, doi:10.1016/S0924-4247(01)00734-8 (2002).

27   Pollack, M. G., Shenderov, a. D. & Fair, R. B. Electrowetting-based actuation of droplets for integrated microfluidics. *Lab on a chip* **2**, 96-101, doi:10.1039/b110474h (2002).

28   Paik, P., Pamula, V. K., Pollack, M. G. & Fair, R. B. Electrowetting-based droplet mixers for microfluidic systems. *Lab on a chip* **3**, 28-33, doi:10.1039/b210825a (2003).

29   Wheeler, A. R. Putting electrowetting to work. *Science* **322**, 539-540 (2008).

30   K. Ugsornrat , T. M., T. Pogfai, A. Wisitsoraat, T. Lomas, A. Tuantranont. Experimental Study of Single-Plate EWOD Device for a Droplet Based peR System. **The 8th Electrical Engineering/ Electronics, Computer,Telecommunications and Information Technology**, 6-9 (2011).

31   M.G. Pollack, P. Y. P., A.D. Shenderog, V.K. Pamula, F.S. Dietrich and R.B. Fair. INVESTIGATION OF ELECTROWETTING-BASED MICROFLUIDICS FOR REAL-TIME PCR APPLICATIONS *7th lnternatatioonal Conference on Miniaturized Chemical and Blochemical Analysis Systems*, 619-622 (2003).

32   Issadore, D., Franke, T., Brown, K. a., Hunt, T. P. & Westervelt, R. M. High Voltage Dielectrophoretic and Magnetophoretic Hybrid Integrated Circuit / Microfluidic Chip. *Journal of microelectromechanical systems : a joint IEEE and ASME publication on microstructures, microactuators, microsensors, and microsystems* **18**, 1220-1225, doi:10.1109/JMEMS.2009.2030422 (2009).

33   Shamai, R., Andelman, D., Berge, B. & Hayes, R. Water, electricity, and between… On electrowetting and its applications. *Soft Matter* **4**, 38, doi:10.1039/b714994h (2008).

34   C. Quillieta, B. B. Electrowetting: a recent outbreak. *Colloid & Interface Science* **6**, 34-39 (2001).

35   Lippmann, G. Relations entre les phénomenes électriques et capillaires. *Ann. Chim. Phys.* **5**, 494 (1875).

36   N. Fortner, B. S. Equilibrium and Dynamic Behavior of Micro Flows Under Electrically Induced

Surface Tension Actuation Forces. *Proceedings of the International Conference on MEMS, NANO and Smart Systems (ICMENS'03)* (2003).

37   Shapiro, B., Moon, H., Garrell, R. L. & Kim, C.-J. C. Equilibrium behavior of sessile drops under surface tension, applied external fields, and material variations. *Journal of Applied Physics* **93**, 5794, doi:10.1063/1.1563828 (2003).

38   Tolman, R. C. The Effect of Droplet Size on Surface Tension. *The Journal of Chemical Physics* **17**, 333, doi:10.1063/1.1747247 (1949).

39   Allen, P. B. *et al.* Selective electroless and electrolytic deposition of metal for applications in microfluidics: fabrication of a microthermocouple. *Analytical chemistry* **75**, 1578-1583 (2003).

40   Tashiro, R. & Sugiyama, H. The molecular-thermometer based on B-Z transition of DNA. *Nucleic acids symposium series (2004)*, 89-90, doi:10.1093/nass/48.1.89 (2004).

41   Jeon, S., Turner, J. & Granick, S. Noncontact temperature measurement in microliter-sized volumes using fluorescent-labeled DNA oligomers. *Journal of the American Chemical Society* **125**, 9908-9909, doi:10.1021/ja036431+ (2003).

42   Chung, G. & Kim, C. RTD characteristics for micro-thermal sensors. *Microelectronics Journal* **39**, 1560-1563, doi:10.1016/j.mejo.2008.02.028 (2008).

43   Brown, A. & Saluja, C. The use of cholesteric liquid crystals for surface-temperature visualisation of film-cooling processes. *Journal of Physics E: Scientific Instruments* **11**, 1068 (1978).

44   Beg, O. U. & Holt, R. G. A cost-effective plasmid purification protocol suitable for fluorescent automated DNA sequencing. *Molecular biotechnology* **9**, 79-83, doi:10.1007/BF02752700 (1998).

45   Kim, J. *et al.* Fabrication and characterization of a PDMS–glass hybrid continuous-flow PCR chip. *Biochemical Engineering Journal* **29**, 91-97, doi:10.1016/j.bej.2005.02.032 (2006).

46   Neuzil, P., Zhang, C., Pipper, J., Oh, S. & Zhuo, L. Ultra fast miniaturized real-time PCR: 40 cycles in less than six minutes. *Nucleic acids research* **34**, e77, doi:10.1093/nar/gkl416 (2006).

47   Qi, H., Wang, X., Chen, T., Ma, X. & Zuo, T. Fabrication and characterization of a polymethyl methacrylate continuous-flow PCR microfluidic chip using CO_2 laser ablation. *Microsystem Technologies* **15**, 1027-1030, doi:10.1007/s00542-009-0843-0 (2009).

48   Ramalingam, N. *et al.* Real-time PCR array chip with capillary-driven sample loading and reactor sealing for point-of-care applications. *Biomedical microdevices*, 1007-1020, doi:10.1007/s10544-009-9318-4 (2009).

49   Sun, Y. *et al.* A lab-on-a-chip device for rapid identification of avian influenza viral RNA by solid-phase PCR. *Lab on a chip*, 1457-1463, doi:10.1039/c0lc00528b (2011).

50   Shin, Y. S. *et al.* PDMS-based micro PCR chip with Parylene coating. *Journal of Micromechanics and Microengineering* **13**, 768-774, doi:10.1088/0960-1317/13/5/332 (2003).

51   Fair, R. B. Digital microfluidics: is a true lab-on-a-chip possible? *Microfluidics and Nanofluidics* **3**, 245-281, doi:10.1007/s10404-007-0161-8 (2007).

52   Lee, D., Chen, P.-J. & Lee, G.-B. The evolution of real-time PCR machines to real-time PCR chips. *Biosensors & bioelectronics* **25**, 1820-1824, doi:10.1016/j.bios.2009.11.021 (2010).

53   Toumazou, C. *et al.* Simultaneous DNA amplification and detection using a pH-sensing semiconductor system. *Nature methods* **10**, 641-646, doi:10.1038/nmeth.2520 (2013).

54   Dickson, J. F. On-chip high-voltage generation in MNOS integrated circuits using an improved voltage multiplier technique. *Solid-State Circuits, IEEE Journal of* **11**, 374-378 (1976).

55   Pylarinos, L. Charge Pumps : An Overview. *Proceedings of the IEEE International Symposium on Circuits and Systems* (2003).

56   Richard, J.-F. & Savaria, Y. High voltage charge pump using standard CMOS technology. *The 2nd Annual IEEE Northeast Workshop on Circuits and Systems, 2004. NEWCAS 2004.*, 317-320, doi:10.1109/NEWCAS.2004.1359095 (2004).

57   Hoque, M. R., McNutt, T., Zhang, J., Mantooth, a. & Mojarradi, M. A high voltage Dickson charge pump in SOI CMOS. *Proceedings of the IEEE 2003 Custom Integrated Circuits Conference, 2003.*, 493-496, doi:10.1109/CICC.2003.1249448.

58   Shin, J., Chung, I.-y., Park, Y. J. & Min, H. S. A new charge pump without degradation in threshold voltage due to body effect [memory applications]. *IEEE Journal of Solid-State Circuits* **35**, 1227-1230, doi:10.1109/4.859515 (2000).

59   Cova, S., Ghioni, M., Lacaita, A., Samori, C. & Zappa, F. Avalanche photodiodes and quenching circuits for single-photon detection. *Applied Optics* (1996).

60   Field, R. M., Lary, J., Cohn, J., Paninski, L. & Shepard, K. L. A low-noise, single-photon avalanche diode in standard 0.13 µm complementary metal-oxide-semiconductor process. *Applied Physics Letters* **97**, 211111, doi:10.1063/1.3518473 (2010).

61   Gersbach, M. *et al.* A low-noise single-photon detector implemented in a 130nm CMOS imaging process. *Solid-State Electronics* **53**, 803-808, doi:10.1016/j.sse.2009.02.014 (2009).

62   Stoppa, D., Mosconi, D., Pancheri, L. & Gonzo, L. Single-Photon Avalanche Diode CMOS Sensor for Time-Resolved Fluorescence Measurements. *IEEE Sensors Journal* **9**, 1084-1090, doi:10.1109/JSEN.2009.2025581 (2009).

63   Richardson, J. A., Member, G. S., Grant, L. A. & Henderson, R. K. A Low Dark Count Single Photon Avalanche Diode Structure Compatible with Standard Nanometer Scale CMOS Technology. 8-11 (2009).

64   Rae, B. R. *et al.* A CMOS Time-Resolved Fluorescence Lifetime Analysis Micro-System. *Sensors* **9**, 9255-9274, doi:10.3390/s91109255 (2009).

65   Shaw, J. M., Gelorme, J. D., LaBianca, N. C., Conley, W. E. & Holmes, S. J. in *IBM Journal of Research and Development* Vol. 41   81-94 (1997).

66   LaBianca, N. C. & Gelorme, J. D. High-aspect-ratio resist for thick-film applications. *Proceedings of SPIE* **2438**, 846 (1995).

67   Bogdanov, A. L. Use of SU-8 negative photoresist for optical mask manufacturing. *MAX-Lab, University of Lund, SE-221 00, Lund, Sweden* (1996).

68   Hammond, P. & Cumming, D. Encapsulation of a liquid-sensing microchip using SU-8 photoresist. *Microelectronic engineering* **73**, 893-897 (2004).

69   Jeon, S., Turner, J. & Granick, S. in *Journal of the American Chemical Society* Vol. 125   9908-9909 (2003).

70   Tashiro, R. & Sugiyama, H. The molecular-thermometer based on BZ transition of DNA. *Nucleic Acids Symposium Series* (2004).

71   Markham, N. R. & Zuker, M. DINAMelt web server for nucleic acid melting prediction. *Nucleic Acids Research* **33**, W577-W581, doi:10.1093/nar/gki591 (2005).

72   Alexandrov, a. D. & Avramov, M. Z. Nucleation from supersaturated water vapors onn-dodecane substrate: A reverse Wilson chamber (RWC) method study. *Colloid & Polymer Science* **271**, 162-172, doi:10.1007/BF00651819 (1993).

73   Group, B. G., Billiton, B. H. P., International, C. N. R., Uk, M. O. & Uk, S. OIL-IN-WATER ANALYSIS METHOD (OIWAM) JIP A Final Report for A Final Report for. (2005).

74   Sakiadis, B. C. & Coates, J. Prediction of specific heat of organic liquids. *AIChE Journal* **2**, 88-93, doi:10.1002/aic.690020119 (1956).

75   Osborne, K. Determining the Contact Angle of a Droplet on a Substrate. *Program*, 1-32 (2008).

76   Yoon, J.-Y. & Garrell, R. L. Preventing Biomolecular Adsorption in Electrowetting-Based Biofluidic Chips. *Analytical Chemistry* **75**, 5097-5102, doi:10.1021/ac0342673 (2003).

77   Lu, S., Abseher, R. & Schreiber, H. The Temperature-Dependence of Hydrophobic Association in Water. Pair versus Bulk Hydrophobic Interactions. **7863**, 4206-4213 (1997).

Appendix

6

7.1 SU-8 thick film IC Encapsulation Process Flow

Figure 7-1: Nitric acid passivation etch to remove polyimide and silicon nitride
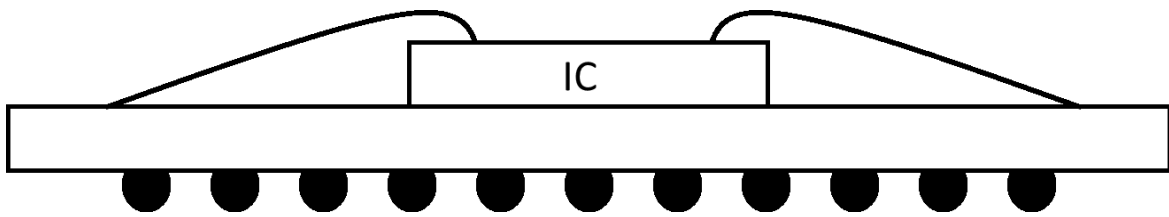
Figure 7-2: Wirebonding the IC to the BGA 272 package
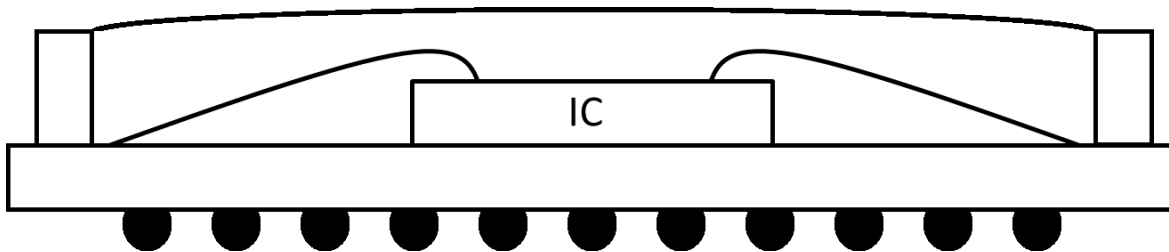
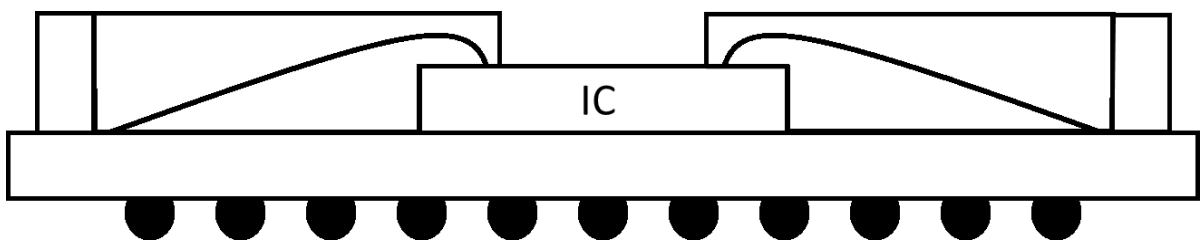Figure 7-3: SU-8 2100 application around wirebonded IC bounded by a PEN guard ring

Figure 7-4: Fully patterned SU-8; wirebonds protected while center of chip is exposed
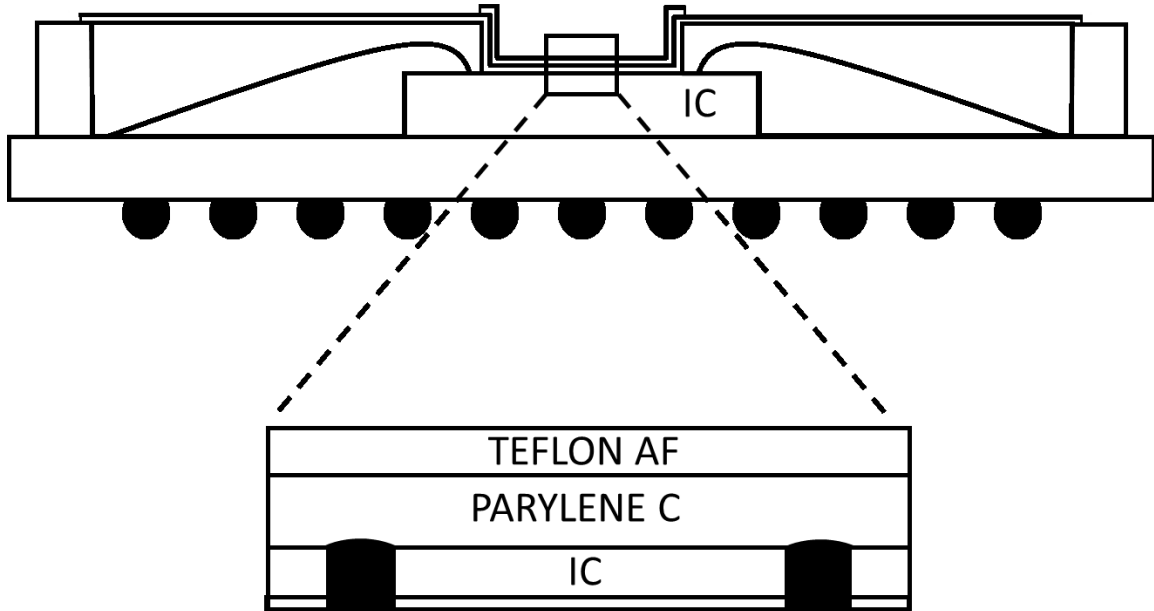
Figure 7-5: Final stack with Parylene C (thermal evaporation) and Teflon AF (spin-coated)

7.2 Time-resolved Demonstration of DNA Thermometer on thin-film metal strip

The following time lapse heat map demonstrates the use of DNA as a spatially resolved thermometer. The device under test is a chrome trace on glass whose width is 50μm and length is 1cm. The time between each image is 30sec with an exposure time of 100ms. The voltage applied across the trace is held constant at 8V, drawing an average of 44mA over the course of the experiment. The chrome trace reaches the linear region of the DNA thermometer's melting curve at about 13 seconds into after applying the voltage to the device.
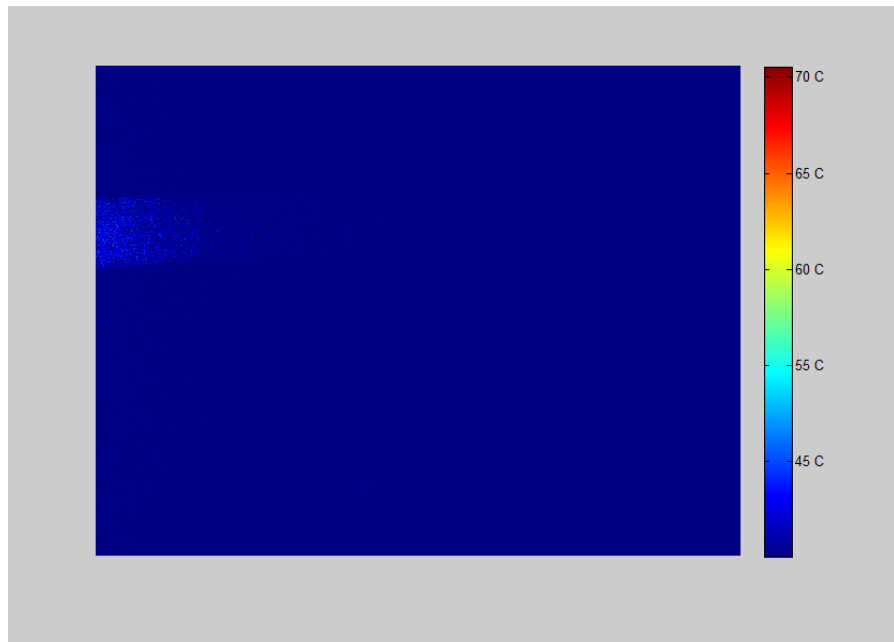
Figure 7-6: DNA thermometer demonstration - T = 13 seconds
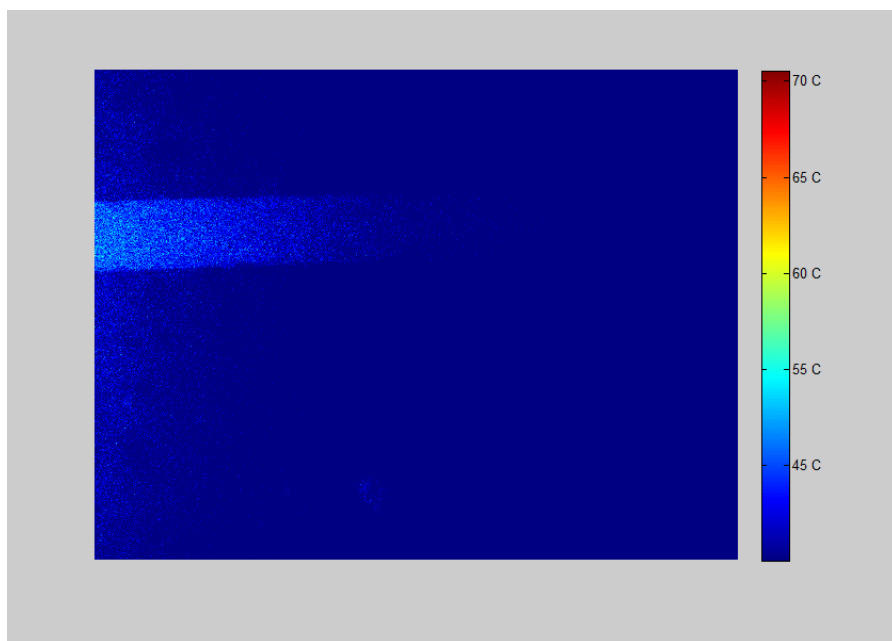
Figure 6-7: DNA thermometer demonstration - T = 15 seconds
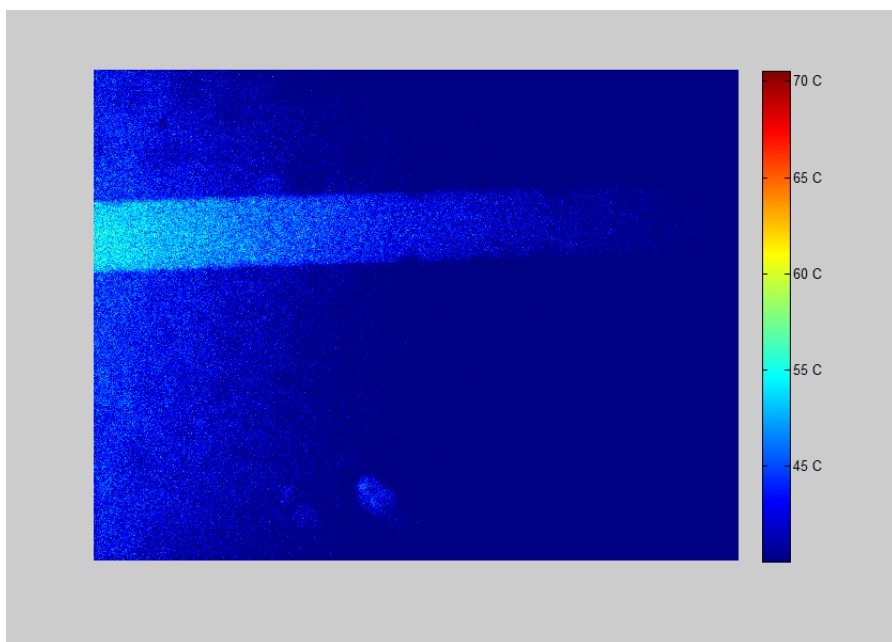
Figure 7-8: DNA thermometer demonstration - T = 17 seconds
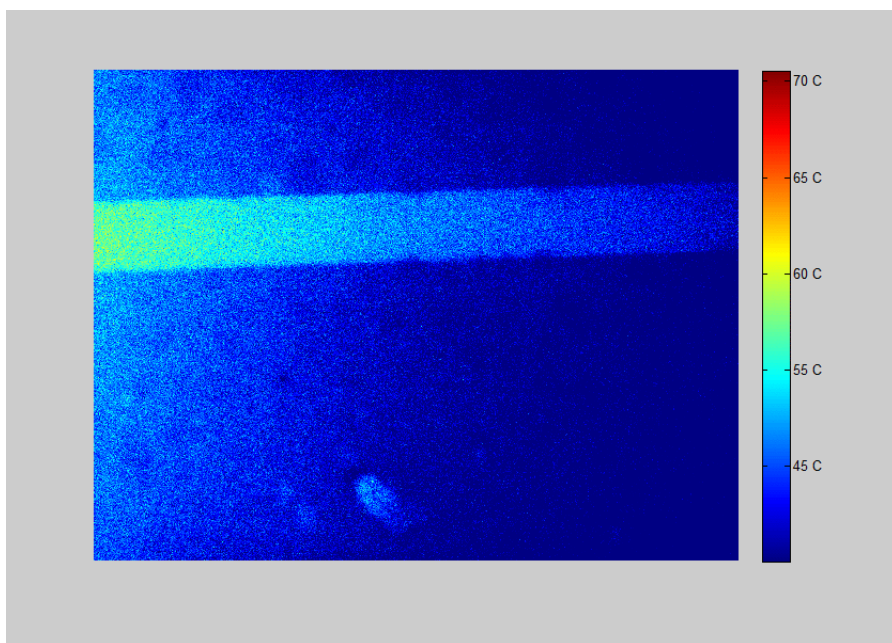
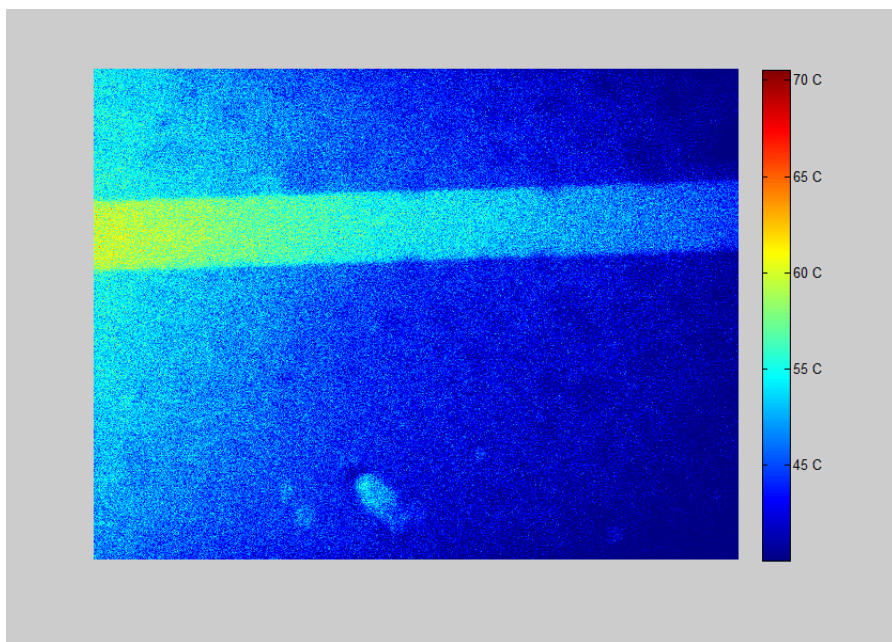Figure 7-9: DNA thermometer demonstration - T = 19 seconds

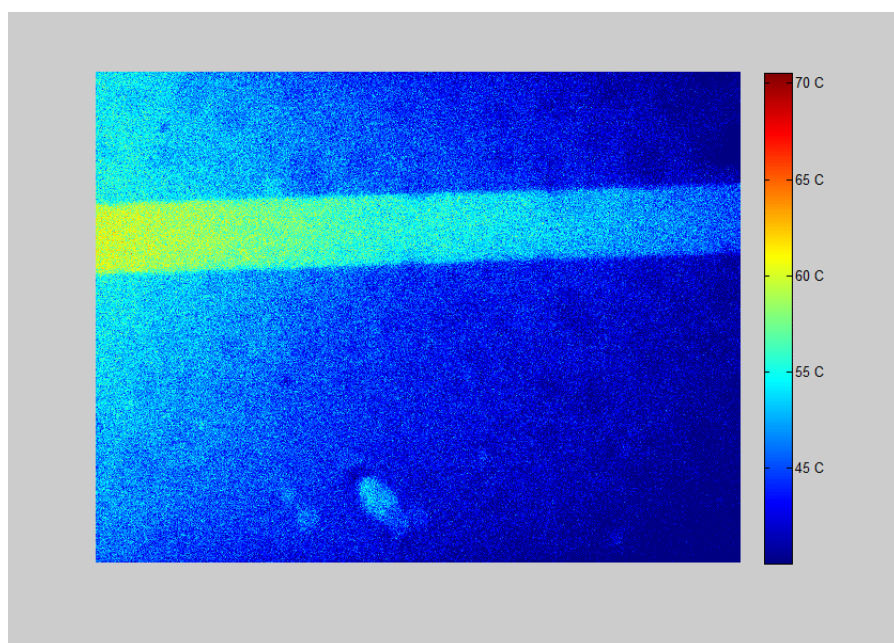Figure 7-10: DNA thermometer demonstration - T = 21 seconds

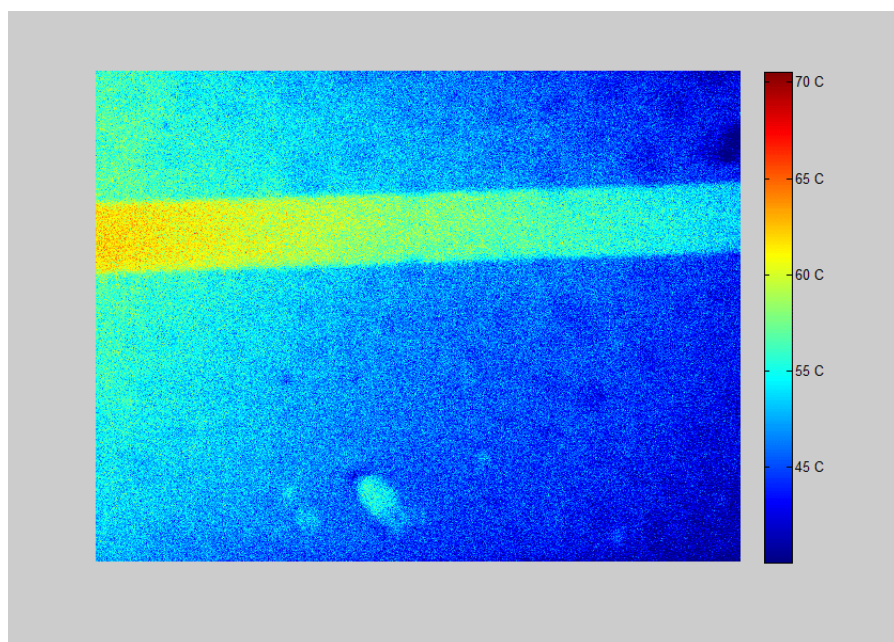Figure 7-11: DNA thermometer demonstration - T = 23 seconds

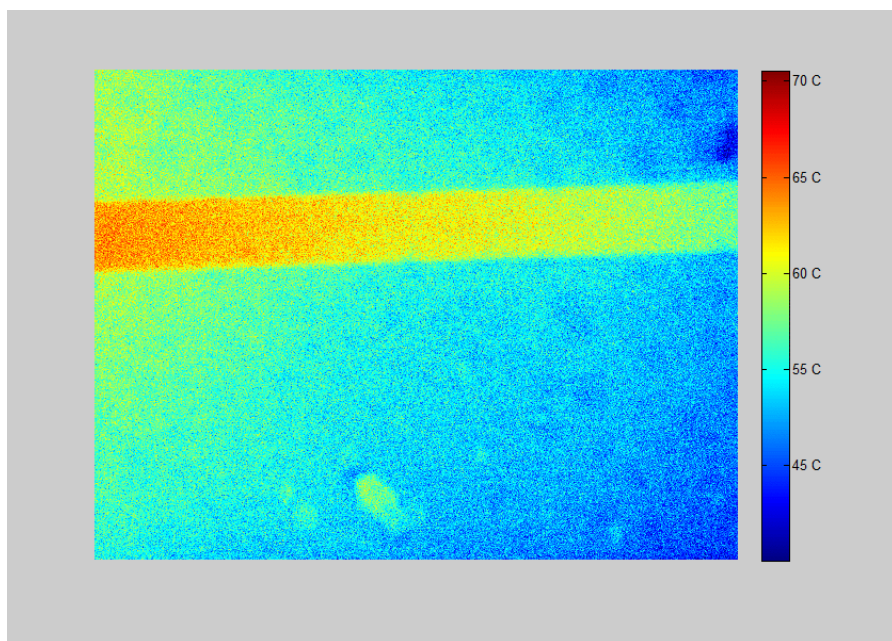Figure 7-12: DNA thermometer demonstration - T = 25 seconds
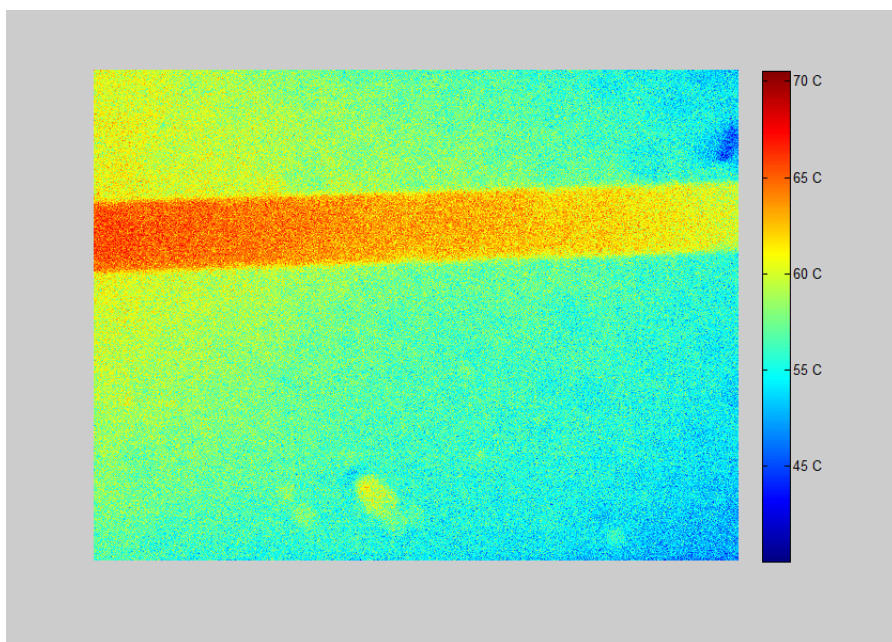
Figure 7-13: DNA thermometer demonstration - T = 27 seconds

Figure 7-14: DNA thermometer demonstration - T = 29 seconds